FINAL REPORT FOR AWARD NUMBER: DE-NE0000704

AWARDEE NAME: University of California Davis

The objective of this project was to develop robust, high-efficiency materials for capture of fission product gases such as He, Xe and Kr in scenarios relevant for both reactor fuels and reprocessing operations. The relevant environments are extremely harsh, encompassing temperatures up to 1500 °C, high levels of radiation, as well as potential exposures to highly-reactive chemicals such as nitric acid and organic solvents such as kerosene. The requirement for nanostructured capture materials is driven in part by the very short (few micron) diffusion distances for product gases in nuclear fuel.[1-2] We achieved synthesis, characterization and detailed modeling of the materials. Although not all materials reviewed in this report will be feasible for the ultimate goal of integration in nuclear fuel, nevertheless each material studied has particular properties which will enable an optimized material to be efficiently developed and characterized.

Below we describe in detail the achievements in the different areas

EXPERIMENTAL REACTOR SET UP AND SYNTHESIS APPROACH

Experimental set-up construction and testing of furnace reactor

The experimental reactor was constructed in the beginning of the project (July 2014) and reaction, testing and synthesis were carried out subsequently. For the reactor an alumina tube furnace from MTI (Model GSL 1700X-60) was used to carry out the reaction. The furnace reactor specifications are listed in Table 1 below. Figure 1 shows a picture of the furnace reactor with the inlet, outlet, flow meter, and vacuum pump labeled.

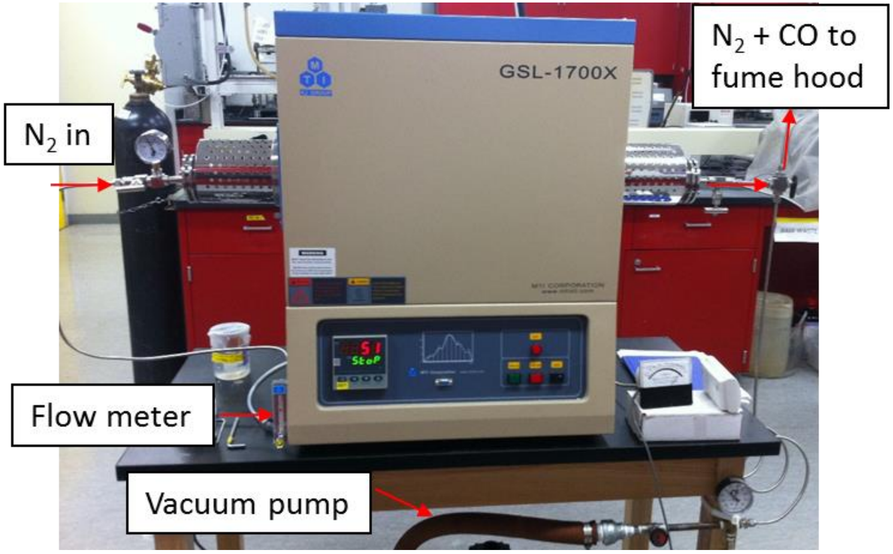

Figure 1: Experimental set-up of the alumina tube furnace reactor assembled for the project.

Table 1: Furnace reactor specifications

	GLS-1700X-60
Max power	4.8 kW
Voltage	220 V AC
Max working temperature	1700 ˚C (< 1 h)
Continuous working temperature	800-1600 ˚C
Max heating/cooling rate	5 ˚C/min
Max gas flow rate	200 mL/min
Heating zone	457 mm
Constant temperature zone	150 mm
Dimensions	590 mm (L) x 490 mm (W) x 760 mm (H)
Weight	160 kg

The crucible is placed in the middle of the alumina tube, inside the heating zone. In Figure 2, we can see a diagram of the different zones of the furnace reactor. The thermoblocks on both sides of the zone prevent heat transfer to the surroundings and extend the lifetime of the tube and parts.

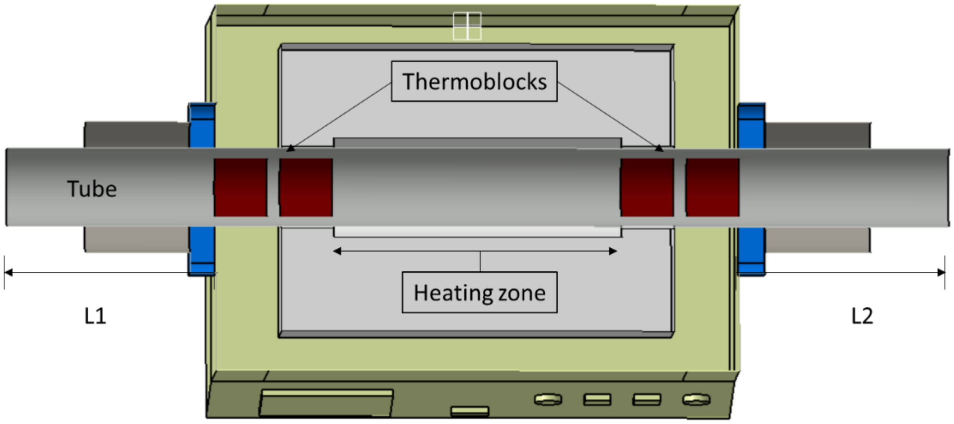

Figure 2: Diagram of the alumina tube furnace reactor.

Reaction progression with temperature

After placing the crucible containing the reactants into the heating zone, the tube is sealed and evacuated using the vacuum pump. Once fully evacuated, the chamber is filled with nitrogen. The reactants are then heated from 200 ºC to 800 ºC at 10 ºC/min and from 800 ºC to 1500 ºC at 5 ºC/min. The reaction is held at 1500 ºC for 30-60 min under a nitrogen flow rate of 40-120 mL/min [3] . The reaction progression with temperature is shown in Figure 3 [4].

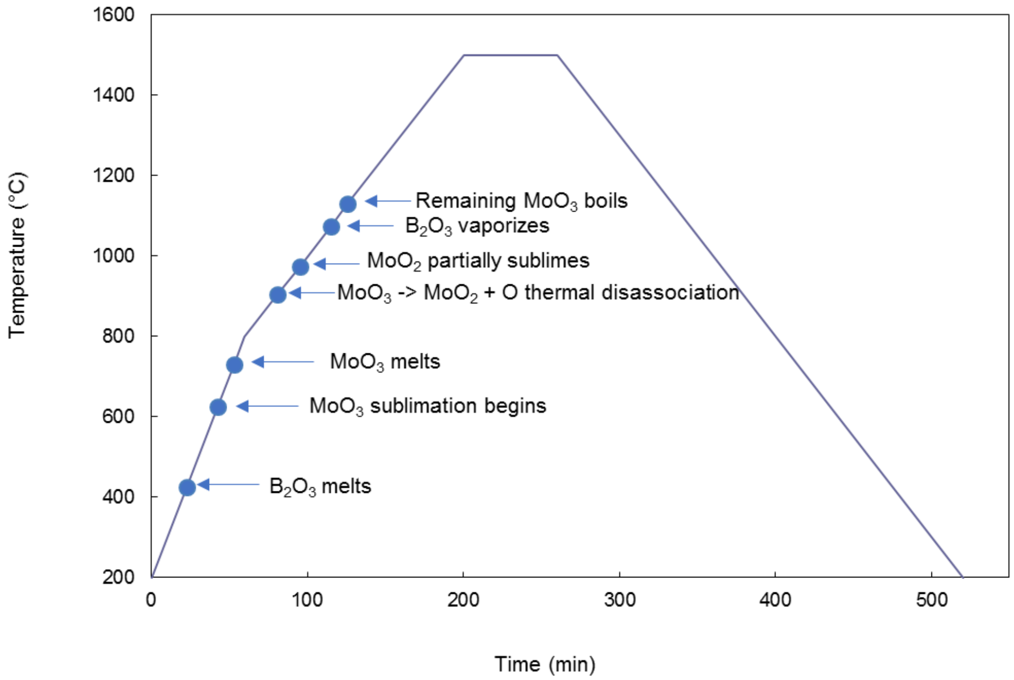

Figure 3: Reactor temperature profile.

BNNT synthesis

Boron nitride nanotubes and molecular sieves were synthesized via a substitution reaction using carbon templates with B_2O_3 in the presence of a MoO_3 promoter and flowing nitrogen atmosphere. B_2O_3, MoO_3, and the carbon template were combined in a 5:2:1 mass ratio, respectively [4]. The reactants were placed in a crucible and heated to temperatures up to 1500 ˚C under various nitrogen flow rates. Single walled carbon nanotubes of diameters ranging from 0.8-1.6 nm and carbon molecular sieves were used as template materials for the boron nitride nanotube and molecular sieve synthesis, respectively.

Figure 4 shows the crucible with the reactants inside – the mixture of B_2O_3/MoO_3 was placed at the bottom of the crucible and the carbon material was placed on top. This placement was to ensure that boron oxide vapor rises up to react with the carbon and flowing nitrogen. The first set of reactions were run in an alumina crucible. Boron nitride crucibles were later used to prevent alumina contamination in the product.

Figure 4: Diagram and picture of the crucible with the reactants inside.

CHARACTERIZATION OF COMMERCIAL MATERIALS

We characterized the commercial CMS, CNT, and BNNT materials to use as a comparison with our synthesized products.

Single walled nanotubes (CNT).

The commercial carbon nanotubes used as the template are single wall carbon nanotubes (product 0550CA) from SkySpring Nanomaterials, Inc. The material purity is listed as > 95 wt% carbon nanotubes and > 90 wt% single walled nanotubes. The outside diameter is between 1 and 2 nm, the inside diameter is between 0.8 and 1.6 nm, and they are 5-20 µm long. The nanotubes have a specific surface area of at least 400 m^2/g and were manufactured by catalytic CVD.

The commercial CNT were analyzed using the high-resolution NanoSEM. Figure 5 shows two pictures obtained at different magnifications. In the left hand picture, we can resolve bundles of tubes with a bundle diameter of about 20 nm. Individual nanotubes cannot be resolved on the SEM and require a TEM to achieve an image on the sub-nanometer scale.

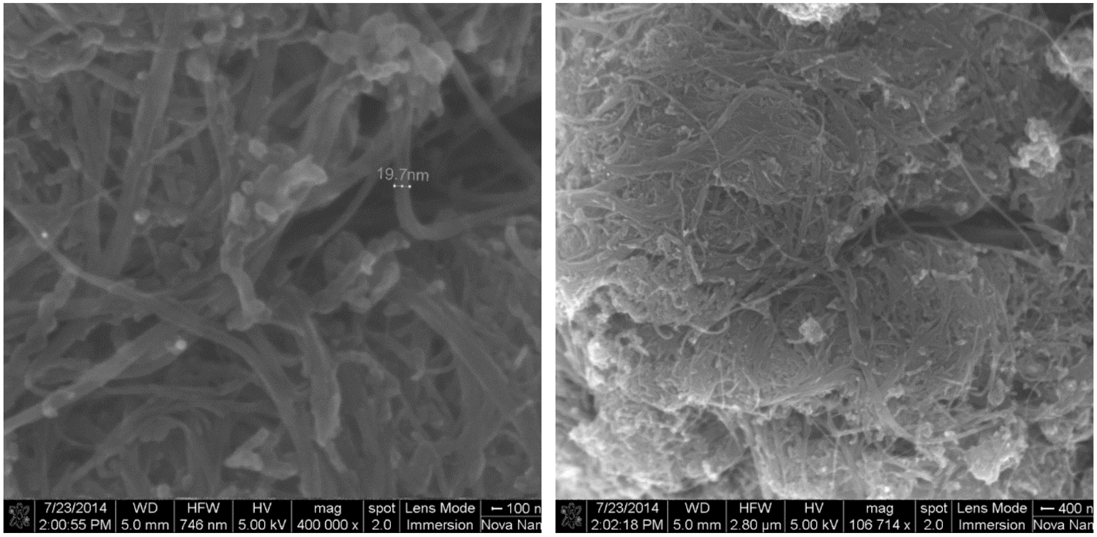

Figure 5: SEM picture of commercial SWCNT at different magnification. Left image taken at 400Kx. Right image taken at 100Kx.

To determine the composition of the commercial CNT, EDS analysis was conducted. The EDS results (Table 3) show that the majority of the composition is carbon, as expected. However, there is a small quantity of oxygen. The results show that almost the 95% of weight are carbon, which is in agreement with the product info.

Table 3: EDS results for a commercial CNT

ELEMENT	% WEIGHT
C	94.76
O	5.24

Figure 6 shows the XRD pattern and its peaks labeled with the corresponding carbon planes. The peak of (002) plane is much sharper compared to that of the CMS material, which confirms the CNTs are more ordered and crystalline. The results are consistent with the spectrum obtained for others sources [6].

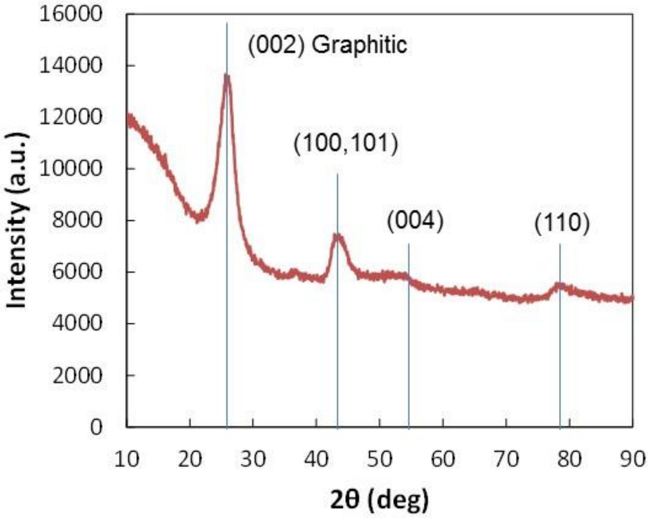

Figure 6: XRD spectrum of commercial CNT

Commercial BNNT

Commercial BNNT were obtained from BNNT, LLC and have a purity of 40-50% of weight. The impurities are hBN (hexagonal form of BN) flakes and elemental boron particles. The nanotubes are 1-5 walls thick and have a length of up to 200 microns. The BET surface area is report to be about 300 m^2/g.

Figure 7 shows SEM pictures that were taken at 5 kV at two different magnifications. The images show some charging effects due to the fact that the sample was not coated. Unlike the carbon materials, BN materials have a band gap in the semiconducting range and can cause charging effects when viewed in an electron microscope. To prevent this in the future, the material will be coated with a thin, conductive layer of Au-Pd.

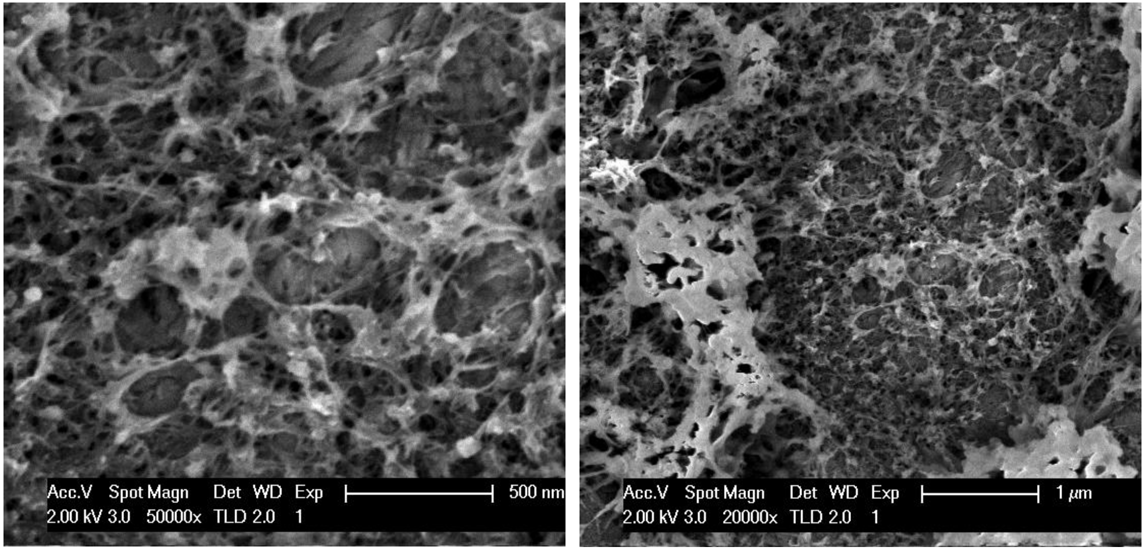

Figure 7: SEM picture of commercial BNNT at different magnification. Left image taken at 50,000×. Right image taken at 20,000×.

Table 4 shows the EDS results of the commercial BNNT. The majority of the sample is boron at 53.84 wt%, with a smaller amount of nitrogen at 15.08 wt%. We can also see that there is a significant amount of carbon and oxygen. The ratio of B:N in BNNT should be 1:1, however the results show a ratio of almost 5:1. This is most likely due to the presence of hBN and B particles, as well as the presence of B_2O_3 , which would explain the quantity of oxygen. The source of carbon is still unknown, but could be due to improper sample preparation.

Table 4: EDS results of commercial BNNT

ELEMENT	% WEIGHT	% ATOMIC
B	53.84	58.23
C	26.61	25.91
N	15.08	12.59
O	4.47	3.27

TEM analysis was carried out to determine the nanotube dimensions. Nanotubes were dispersed in methanol, sonicated for 1 minute, and dropped onto a holey carbon grid. The multi-walled BN nanotubes have an ID between 1-4 nm and wall thicknesses of approx. 2 nm (Figure 8). There are also some nanoparticles, most likely hBN, about 10-15 nm wide, as seen in the left hand figure. The features around the individual nanotube in the right hand picture may be a result of solvent interactions.

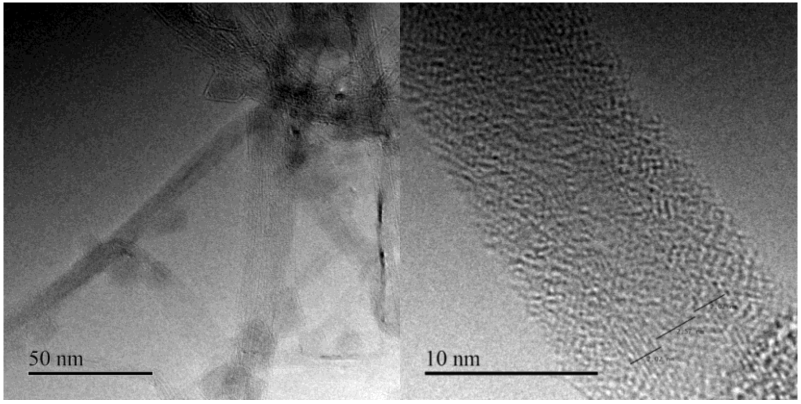

Figure 8: TEM pictures of commercial BNNT

Gas Adsorption Studies

Adsorption measurements in all materials were carried out in order to determine the adsorptive properties, surface area and pore size, of our materials.

Procedure.

The adsorption capability and porosity of various samples were studied using the Micromeritics Gemini VII 2390 Surface Area Analyzer. A small amount (20-60 mg) of the CMS and BNNT were degassed under vacuum at 250 C for at least 18 hours prior to each measurement. Zeolite samples were degassed under vacuum at 400 C for at least 18 h prior to each measurement.

Carbon molecular sieves (CMS)

The N_2 adsorption of the commercial CMS material was extensively studied. Initial tests on the as-received pellet showed very little adsorption at 77 K, which was attributed to the small pore size of the material. However, later tests with a ground powder showed significantly more adsorption as we can see in Figure 9.

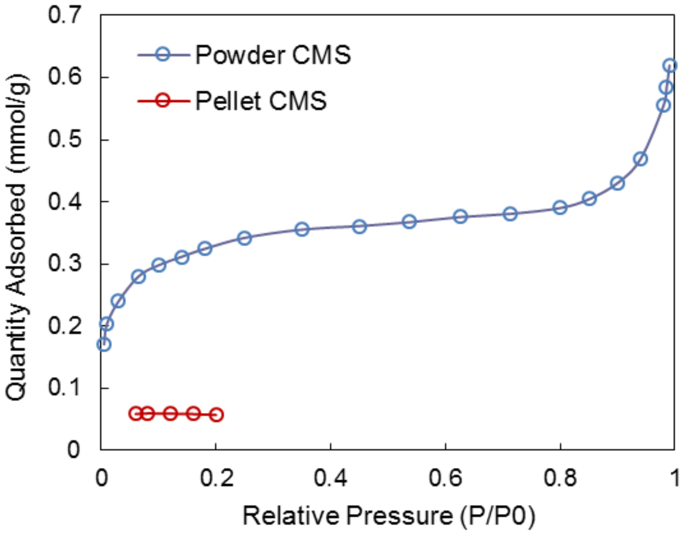

Figure 9. N_2 adsorption of CMS powder and pellet at 77 K.

The enhanced adsorption can be attributed to the fact that grinding the pellet exposes more surfaces for onto which gas molecules can adsorb. The same surfaces in the pellet may have been harder for N_2 to reach, possibly due to kinetic and/or mass transfer limitations.

Since our primary interest is in gas capture at elevated temperatures, we performed N_2 adsorption experiments at room temperature and 673 K as well. These results are shown in Figure 10. At both temperatures, the sample adsorbed approximately 0.37 mmol/g at atmospheric pressure. However, the shape of the isotherms are quite different, with the 298 K isotherm displaying a much more linear profile.

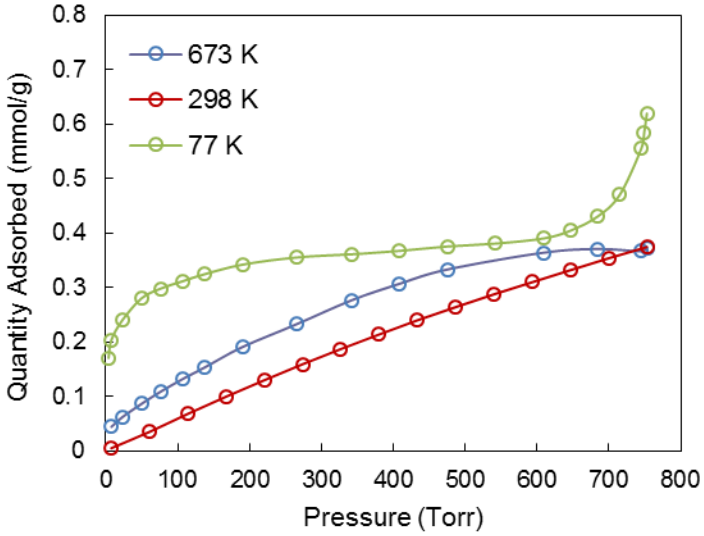

Figure 10. N_2 adsorption of CMS powders at 77 K, 298 K, and 673 K.

At 673 K, the higher temperature provides additional kinetic energy to the nitrogen molecules. In the typical case of adsorbate molecules interacting with the surface, an increase in temperature would lead to a decrease in adsorption. In our microporous system, the additional energy can help the nitrogen overcome any diffusional barriers as it enters the micropores. However, this trend contradicts the results reported by Rutherford in 2005 on nitrogen adsorption experiments from 20 to 80 ˚C and at pressures up to 1600 torr [7]. At higher temperatures, they observed less nitrogen adsorption and more linear behavior. Another possible explanation is that at 673 K, which is well above the temperatures tested by Rutherford, any surface hydroxyl groups on the material may be removed, therefore altering the pore size and structure of the material [8]. This can then affect the adsorption profile as a result.

CO_2 adsorption was also measured to characterize the micropore distribution in the material, as presented in the Figures 11 and 12.

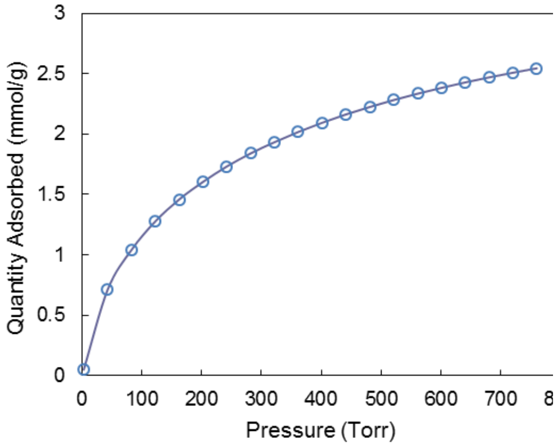

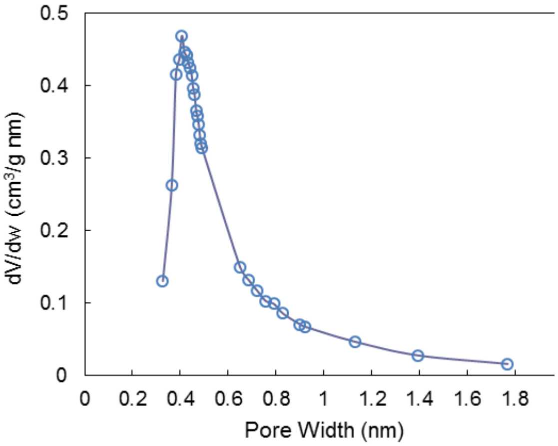

Figure 11. CO_2 adsorption of CMS powder at 77 K, adsorption isotherm

Figure12: CO_2 adsorption of CMS powder at 77 K, differential pore volume

Commercial BNNT

The commercial BNNT was analyzed using N_2 adsorption at 77 K to obtain a BET surface area of 256 m^2/g, which is in agreement with the company's reported values (around 300 m^2/g). The adsorption profile is shown in Figure 13. The adsorption profile suggest multilayer adsorption on the BNNT surface.

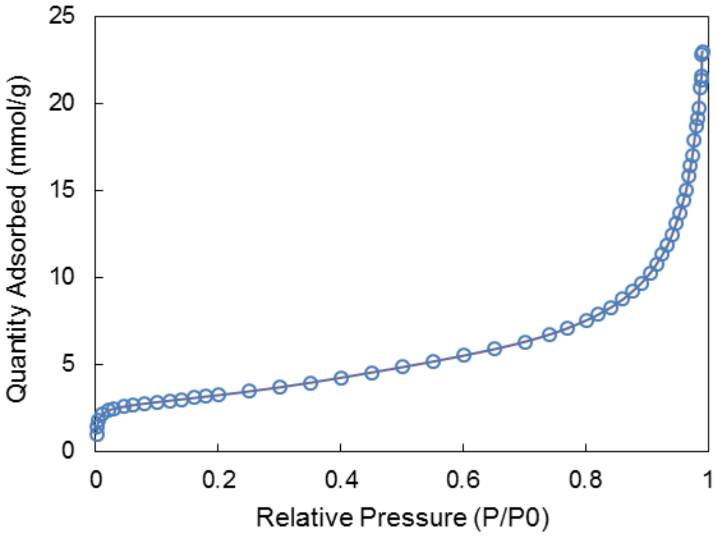

Figure 13. N_2 adsorption of commercial BNNT at 77 K.

In Table 5, we can compare the results obtained for the commercial CMS and BNNT. Because the BNNT sample is composed of a mixture of nanotubes and nanoparticles, the pore size value cannot be accurately determined in the bulk material. Nanotubes have a measureable pore size and a higher surface area compared to nanoparticles. This also may explain why the BET surface area of the CNT (> 95% nanotubes) is higher than that of the BNNT (50% nanotubes).

Table 5: Different adsorptive properties of the CMS and BNNT

Material	**% Mass loss after degas**	**BET surface area (m^2/g)**	**Pore size (nm)**
CMS	2.0	326	0.47
BNNT	4.4	256	-

SYNTHESIZED MATERIALS

Table 6 present the reaction conditions and B/N ratio obtained from Energy Dispersive Spectroscopy (EDS) measurements for commercial BNNT samples. All EDS measurements were taken at 5 keV and a dead time between 20-40%. The starting commercial material has a B/N atomic ratio of 5.0, which indicates a large amount of elemental boron in the sample. To obtain pure BNNTs, there should be equal amounts of B and N.

Table 6: Reaction conditions and B/N ratios for the different BNNT samples. BNNT-com refers to the commercial material, while BNNT-x (x=1-5) refers to different synthesized samples.

Sample	**Temperature (°C)**	**Hold time (min)**	**N_2 Flow rate (mL/min)**	**Crucible**	**B/N atomic ratio**
BNNT-com	-	-	-	**-**	**5.0**
BNNT-1	1500	30	40	Alumina	**6.2**
BNNT-2	1500	30	120	Alumina	**5.4**
BNNT-3	1350	60	120	Alumina	**-**
BNNT-4	1500	60	100	BN	**4.0**
BNNT-5	1450	120	120	BN	**4.8**

Out of the five different batches of synthesized BNNT, BNNT-4 is the most promising sample and has a B/N atomic ratio of 4.0. Increasing the flow rate between BNNT-1 and BNNT-2 samples led to a better B/N ratio as well. BNNT-3, which was synthesized at the lowest temperature and without the Mo promoter, had no detectable boron (no B/N ratio listed). It seems that to obtain a low B/N ratio, one needs to have 1) a high reaction temperature (1500 °C), 2) long hold time, 3) high flow rate, and 4) a BN crucible.

Since the commercial BNNT is reported to contain hBN flakes and elemental B, we conducted a series of oxidation and filtration procedures to isolate the desired BNNT. The BNNT was first oxidized at 800 °C to assist the conversion of hBN and B to B_2O_3, which is water soluble. The sample was then washed with water, and the water-insoluble BNNT was collected using a vacuum filtration method.

Table 7 summarizes the results of the treated commercial BNNT, compared with the as-received commercial BNNT. EDS was taken after oxidation, but before filtration, to assess the effectiveness of each step. While the B/N ratio increases after the oxidation step, the filtration step helps reduce the ratio slightly.

Table 7: Results of treated commercial BNNT. BNNT-com refers to the original commercial BNNT. BNNT-com-1 was partially oxidized. BNNT-com-1f is the filtered result of BNNT-com-1.

Sample	**Oxidation Temp (°C)**	**Hold time (min)**	**Filtered?**	**B/N atomic ratio**
BNNT-com	-	-	-	**5.0**
BNNT-com-1	800	60	No	**5.8**
BNNT-com-1f	800	60	Yes	**5.3**

Current efforts are focused on isolating the BNNT. Dispersing the nanotubes in water or ethanol and sonicating the solution prior to filtration may improve yield.

ZEOLITES

Commercial zeolites NaY and ZSM-5 were obtained for testing and characterization from Zeolyst International. Their corresponding platinum loaded versions at weight % loadings of up to 15% were also obtained. The product information for both zeolites is given in Table 8.

Loading Y-type zeolite with heavy metals has been shown to increase thermal stability [9]. The temperature at which the structure collapses was increased from 882 °C to as much as 973 °C. ZSM-5 zeolite has been shown to undergo decomposition slowly at temperatures over 1000 °C [10]. The combination of the zeolites' thermal stability, high specific surface area, and small pore dimensions makes them a promising material for gas capture applications in nuclear fuel.

Table 8: Product information for commercial zeolites ZSM-5 and NaY

Zeolite	**Nominal Cation Form**	**SiO_2/Al_2O_3 mole ratio**	**Si/Al atomic ratio**	**BET surface area (m^2/g)**	**Pore size (nm)**
ZSM-5	Ammonium	30	15	900	~0.5
NaY	Sodium	5.1	2.6	405	~0.8

SEM/EDS analysis of zeolites

Both zeolites were analyzed with SEM/EDS to determine particle size and confirm the correct Si/Al atomic ratios. The powders were lightly ground, dusted onto double-sided copper tape and then coated with Au-Pd for 2 minutes. All EDS measurements were taken at 5 keV and a dead time between 20-40%.

Initial data showed a significant carbon peak in the spectrum, which was attributed to the carbon-containing adhesive from the tape. From the images, we see that the zeolite particles form a sparse monolayer coverage on the surface. Figure 14 shows two pictures of zeolite NaY at different magnifications and Table 9 shows the EDS results for the same zeolite. The Si/Al ratio for zeolite NaY is 2.5, which is very close to the expected ratio of 2.6. The particles size is between 500 and 800 nm.

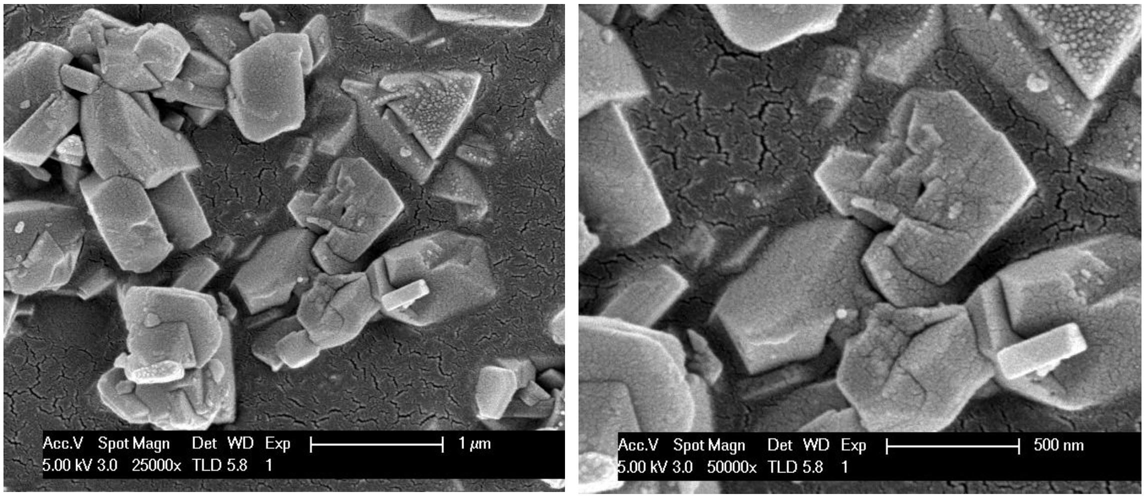

Figure 14: Zeolite NaY. SEM images take at 5 kV at different magnifications. (Au-Pd coating, 2 min)

Table 9. EDS summary for zeolite NaY.

ELEMENT	% ATOMIC
O	48.8
Al	13.01
Si	33.75

Zeolite ZSM-5 was also analyzed for SEM and EDS at the same conditions than NaY. Figure 15 shows two different pictures at different magnification. The particles seem to be irregularly shaped, with the smaller particles measuring ~100 nm. There is a bumpy layer on the sample surface, which was not present in the ZSM-5 specimen. This could be due to sample contamination or a reaction with the environment. Also EDS results for this zeolite are presented in the Table 10. The Si/Al ratio for zeolite ZSM-5 is ~22, which is somewhat high compared to the expected ratio of 15.

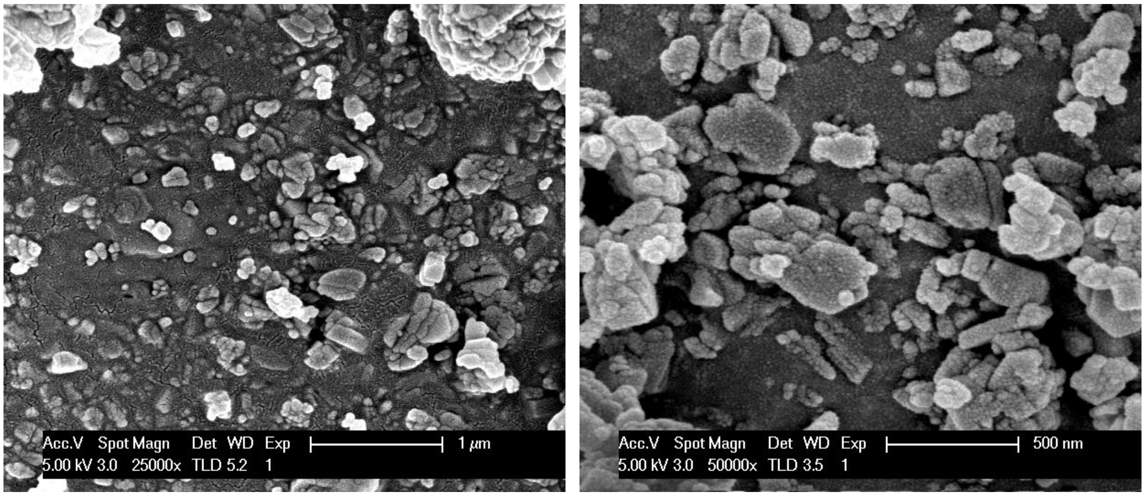

Figure 15: Zeolite ZSM-5. SEM pictures take at 5 kV at different magnifications. (Au-Pd coating, 2 min)

Table 10. EDS report for ZSM-5.

ELEMENT	% ATOMIC
O	47.4
Al	2.24
Si	50.36

Table 11 presents a summary of the Si/Al ratios obtained by EDS for both zeolites.

Table 11: Ratio Si/Al of zeolites ZSM-5 and NaY

Zeolite	Measured	Reported
ZSM-5	21.6	15
NaY	2.5	2.6

Degradation of zeolites at temperatures above 800 °C has been studied. Samples were heated to 800, 1200 and 1500 °C. BET experiments were carried out at room temperature in order to determine the adsorptive properties of the heated zeolites. The surface area decreases with an increase of the treatment temperature. For nitrogen as the adsorptive gas, we can conclude that after heating the samples to 1500 °C, the majority of the porous network has collapsed. ZSM-5-Pt shows slightly better gas adsorption capabilities after heat treatment at 1500 °C than ZSM-5, which suggests that the addition of platinum slightly increases the thermal stability of these materials at high temperatures. BET results suggest that a change in the lattice structure may take place when the material is heated. XRD patterns show that at high temperatures the ZSM-5 transitions to a cristobalite structure.

A model to study the degradation of the zeolites at high temperatures has been developed. The decay of the specific area depends on the treatment temperature and this dependence follows the Arrhenius equation. We obtained a relationship between the surface area and the treatment temperature, which permit prediction of the specific surface area of the zeolite samples exposed to a given temperature. Even though the structure collapses after heat treatment at 1500 C, the zeolites are capable of taking up some helium gas, but not gases with higher molecular weights.

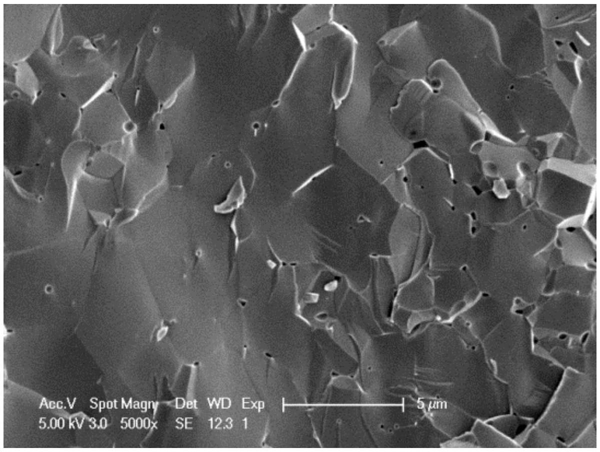

Figure 16: The surface of a sintered pellet made of 8YSZ Tosoh powder

Helium Spectroscopy Measurements on Materials for Noble Gas Retention and Transport in Nuclear Fuel

We treated a range of samples with helium to characterize their retention and transport properties at temperatures relevant for nuclear fuel, up to 1430 ˚C. Samples were yttria-stabilized zirconia (YSZ), nickel substrates (as a surrogate for uranium oxide) coated with alumina by atomic layer deposition, and garnet as a control. Yttria-stabilized zirconia (YSZ) samples were formed from a commercial powder, sintered into dense pellets. YSZ is a promising material for incorporation into nuclear fuel because of its thermal stability and because it is chemically relatively inert. These samples formed from commercial powder were chosen to provide a baseline for future measurements to be performed on nanostructured YSZ particles synthesized at UC Davis. An SEM image of a representative sintered YSZ pellet is shown in Figure 16.

Alumina-coated nickel particles, about 3 micron diameter, were also examined. Alumina is the material of interest for helium sequestration and transport in nuclear fuels, as it has good thermal and chemical stability even at elevated temperatures. A scanning electron microscope (SEM) image of a typical nickel particle is shown in Figure 17 (a). Figure 17(b) and (c) show transmission electron microscope (TEM) image of particle fragments.

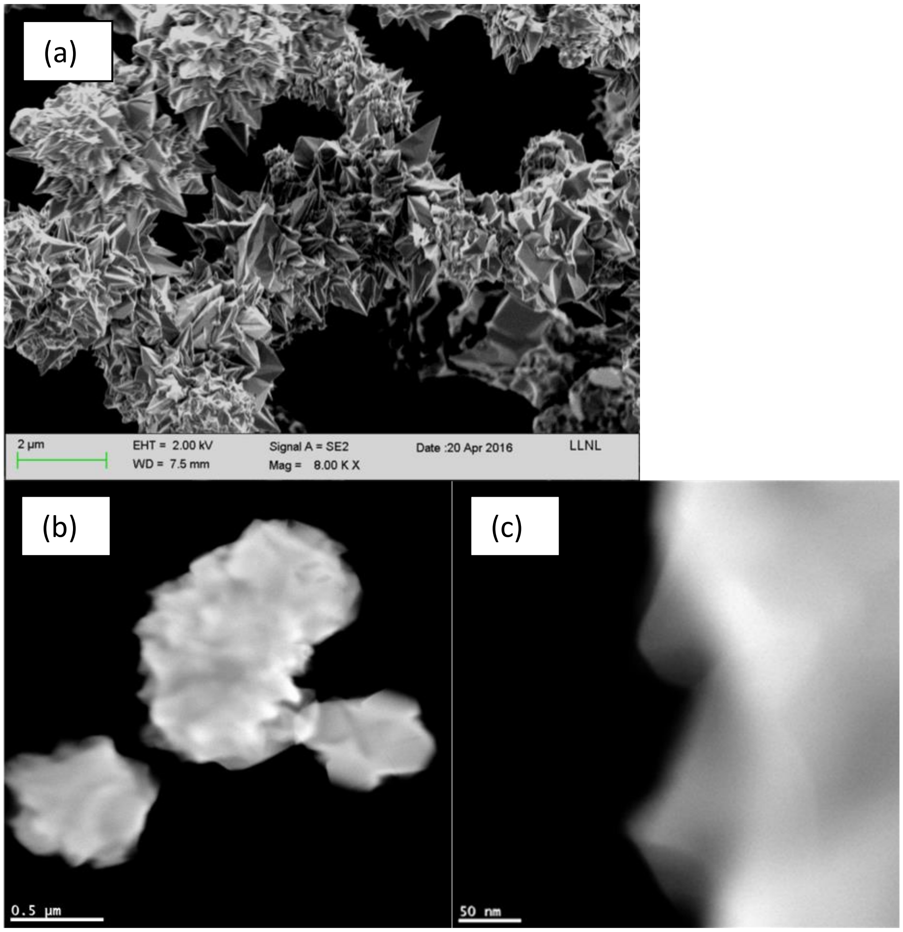

Figure 17: (a) SEM image of nickel particle; (b) and (c): TEM images of Ni particle, with 10 nm alumina coating

Nickel particles were chosen as a substrate to be representative of uranium oxide particles, because like uranium oxide, the nickel particles have very low helium solubility. Fluidized bed atomic layer deposition (ALD) is a promising technique for incorporating this alumina material into nuclear fuel because it is inherently capable of creating uniform, nanostructured coatings on particles. Coatings can be controlled in thickness to a precision of a single atomic layer, and material can be delivered uniformly throughout the fuel if the fuel particles are processed prior to a sintering step.

Finally, garnet was chosen as a control particle because the helium diffusion properties into garnet have been reported in the literature, and therefore measurements made on garnet can be used to characterize our helium loading and measurement processes.

All samples were treated in argon (1 l/m, 800 C, 18 hours) followed by helium (0.5 l/m, 800C, 18 hours). Helium spectrometry was performed with a Nu Instruments Noblesse mass spectrometer at LLNL from 450 to 1430 ˚C. As part of our helium spectrometry measurement process, samples are first brought to elevated temperatures (>200 ˚C) in vacuum, before measurements begin at 450 ˚C.

The total amount of helium observed to evolve from the samples over the temperature range 450 to 1430 C is shown in Figure 18, normalized for sample mass.

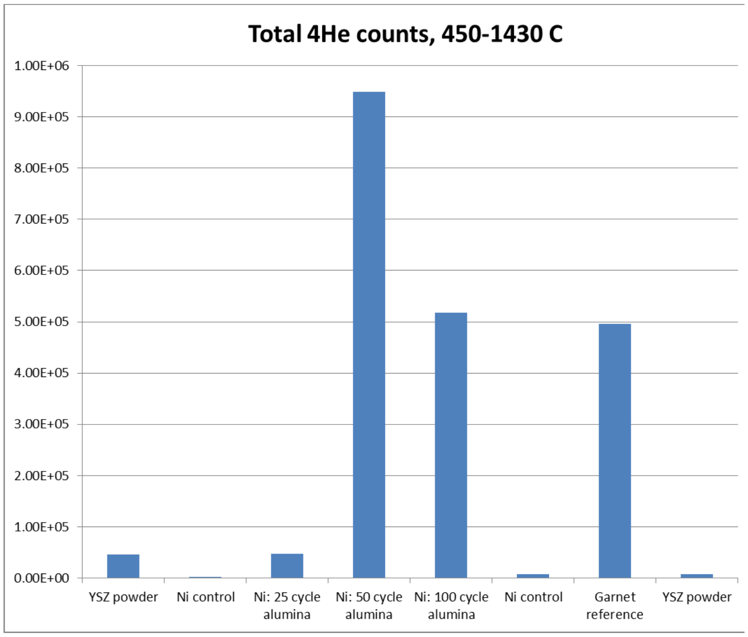

Figure 18. Estimated total 4He counts in tested samples

This data suggests that alumina on the nickel particles can be effective for helium retention and transport. However, it is unclear why the thicker 100 cycle alumina sample has less helium by mass relative to the 50 cycle alumina. One hypothesis is that the alumina is non-uniform as deposited, and that the layers further away from the substrate are less effective at either uptaking or retaining helium.

YSZ is not necessarily ruled out as a useful material for helium retention, since helium could have been released at a temperature below 450 C, the lowest measurement temperature in our helium spectroscopy measurements. In particular, it would be expected that helium could be quickly lost at lower temperatures from porous particles such as those which are being developed for this project. In a nuclear fuel application, however, where YSZ particles are surrounded by impermeable uranium oxide, YSZ particles could still provide a useful helium retention structure.

As a current development in the project, the porous YSZ particles (doped with rare-earths to improve stability) are being mixed with CeO2 (surrogate for UO2) for co-sintering. Because the particles are too big (~300nm), which would make it unpractical in a real system application since particles would take too much volume in the nuclear fuel, the YSZ spheres are being broken using high energy milling to generate small chunks of porous YSZ to be embedded in the CeO2 matrix. Figure 19 shows the results from the milling for 10 min with an irregularly shaped form with the shortest dimension equal 100nm. This is encouraging result but further milling is being conducted to assure sizes below 50nm to allow efficiency mixing with CeO2.

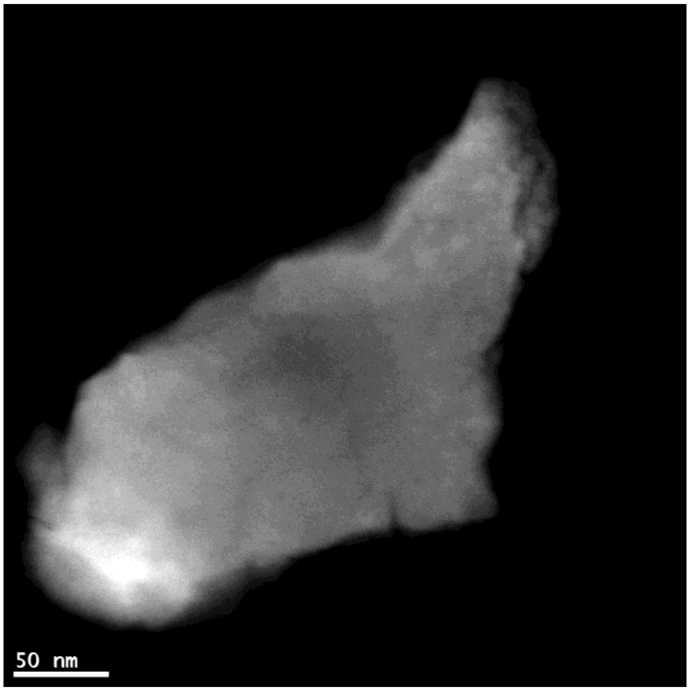

Figure 19 STEM of fragment of milled YSZ porous spheres.

The sintered CeO2 mixed with YSZ porous (broken) spheres will be tested in terms of He adsorption afterwards. At UC Davis, we will use a Thermal Mechanical Analyzer to track the He adsorption effects on the expansion of the pellets as a function of time. The samples will then be studied at LLNL using spectroscopy to quantify adsorption.

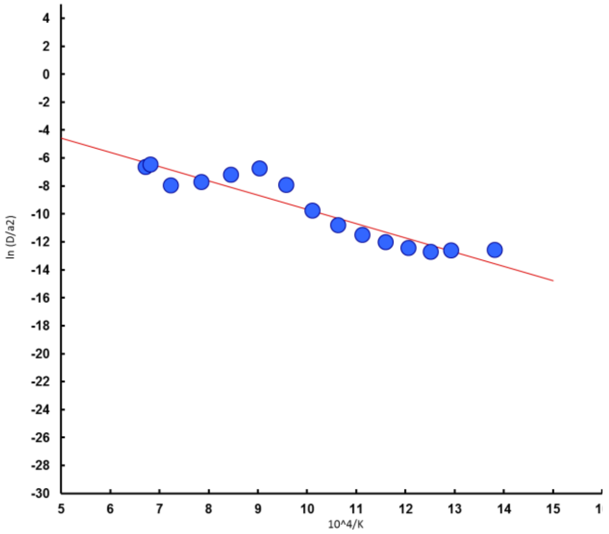

Figure 20. 50 cycle alumina on nickel particles: plot of the natural log of D/a2 vs. reciprocal temperature, where D the diffusion coefficient and a is a characteristic length for diffusion.

In Figure 20, the natural log of the diffusion coefficient is plotted vs. reciprocal temperature, showing a reasonably linear fit for the 50 cycle alumina sample. This data suggests that helium is being transported out of the alumina limited by a thermally-activated process.

Helium generation and diffusion tested samples

The helium concentration $c_{He,fuel}$ in a spent UO_2 fuel pellet, 10.5 g/cm^3, after 300 years is 4.2×10^{19} atoms/cm^3. Furthermore, the diffusion distance of helium in UO_2 at 473 K over 10000 years is just 0.3 µm, while a typical grain diameter is 10 µm. (C. Ferry et al., Journal of Nuclear Materials 407 (2010) 101) This suggests that most helium generated in a UO_2 grain would not migrate to grain boundaries, but would rather remain internally trapped in grains. If UO_2 grains are made smaller than the diffusion distance, however, and each grain is coated in alumina, then the alumina could be a viable transport path or retention volume for helium, depending on the thickness of the alumina. Similarly, helium could be retained in nanostructured YSZ or other particles mixed uniformly with uranium oxide fuel particles.

Mesoporous Silica Nanoparticles (MSN)

We continued the study of the degradation of MSN (type MCM-41) at high temperatures. XRD results show that there is a change in the structure of MSN when we heated this material up to 1500 ^{o}C, which is in agreement with the cristobalite results. Last year (2014) we characterized samples of MCM-41 that had been heat treated at various temperatures up to 1500 C.

We also studied the chemical degradation of MCM-41 in acid. Immersion of MCM-41 into 0.01 M HCl for 24 h at 100 ^{0}C is shown in Table 12.

Table 12. pH conditions before and after boiling 24 hr in 0.01 HCl at 100 ^{o}C.

Solution pH	HCl
Before	2.15
After 24h	1.87

The gas adsorption properties (by BET characterization) were unaffected by the HCL treatment at 100 ^{o}C.

MCM-41 was treated at three different temperatures (500, 1000 and 1500 oC) to study thermal degradation. These temperatures were selected based on the DSC/TGA results. MCM-41 was heated in the presence of air at 10 oC/min to the desired temperature using the Seteram Setsys Evolution 1750 DSC/TGA analyzer. The airflow rate was 20 mL/min. Once the sample achieved the desired temperature, the temperature was cooled at 20 oC/min to room temperature. Fig. 21 shows XRD patterns and adsorption isotherms (here nitrogen) of the systems with and without heat treatment.

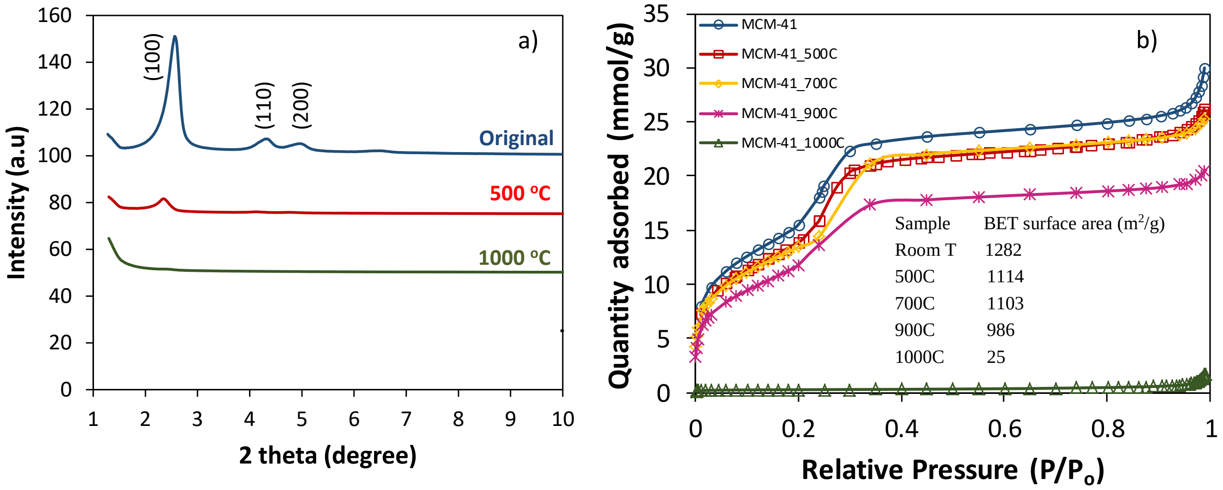

Figure 21. a) XRD patterns of heated MCM-41 samples compared with the untreated sample (original) at room temperature. b) Nitrogen adsorption isotherms at 77 K for the untreated MCM-41 and MCM-41 heated to 500, 700, 900 and 1000 °C. The values for the BET surface areas are given in the Figure.

#1) Synthesis of Yttria-stabilized Zirconia

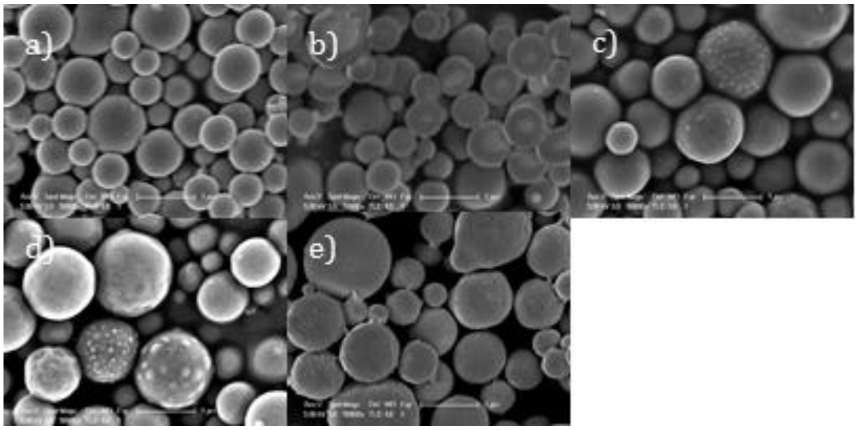

Figure 22 SEM images of YSZ synthesized at different temperatures, a) 700 °C, b) 800 °C, c) 900 °C, d) 1000 °C and e) 1100 °C using PEG in the solution

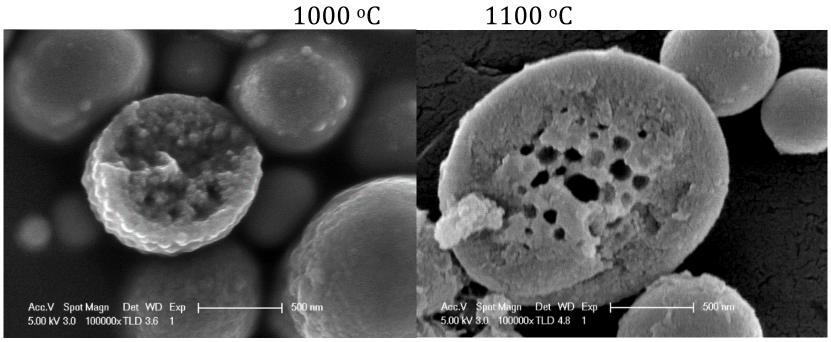

Figure 23 SEM images of YSZ spheres synthesized at 1000 and 1100 °C with PEG

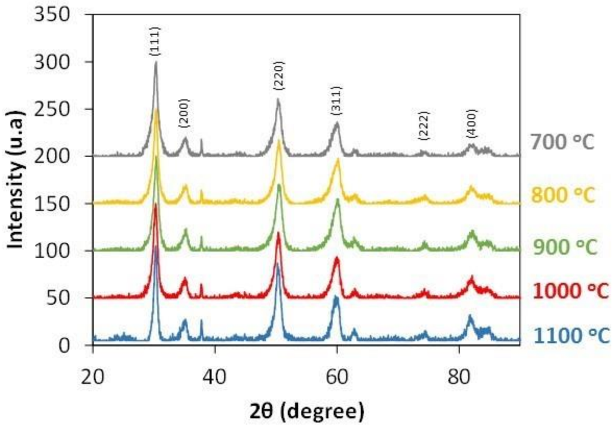

Figure 24 XRD patterns of YSZ synthesized at different temperatures using PEG in the solution.

Yttria-stabilized zirconia (YSZ) has been synthesized by Ultrasonic Spray Pyrolysis at different temperatures (700, 800, 900, 1000 and 1100 °C) using a template in a solution of PEG (Polyethylene glycol ether). The solution is composed by 10% Yttria: 0.164 mol of Zirconium (IV) oxynitrate hydrate 99%, 0.036 mol of Yttrium (III) nitrate hexahydrate 99.9% in water and 11 g of PEG. Figure 22 shows SEM images of YSZ synthesized at different temperatures. The images show spherical nanoparticles with diameters between 500-800 nm. Most of the spheres have a smooth surface. However there are some of them that have some imperfection in the surface (see Fig. 22 c-e). This may be due to the residual surfactant, PEG, from the solution. Figure 23 shows two broken spheres synthesized at

1000 and 1100 °C where the porous inside of the spheres are shown. XRD results, Figure 24, show a typical pattern of cubic YSZ for the material that was synthesized at all temperatures. However, the material becomes more crystalline when the temperature of the synthesis increases. TEM was performed to determine the structure inside of the spheres. TEM images for the YSZ synthesized at 700 and 1100 °C, with different solutions that we have employed, using water as a solvent, using water and ethanol as a solvent and the last one using a surfactant, PEG. TEM images are shown in Figure 25. We can see that the spheres synthesized at 1100 °C show a porous structure – of particular interest for the He capture concept.

Obtaining porous YSZ microspheres with a method that can be scaled up represents a major achievement of the project, and has been submitted for publication. USP is typically expected to produce solid microparticles, but we were capable of modifying the process using high speed flow to control crystallization and allow a porosity to form. Upon thermal stability tests, we have learned that these the porous structure is unstable at high temperatures (above 900°C). That is, although the phase stability is maintained, pores shrink due to sintering, leading to a dense structure. To solve this problem, we have added rare-earth dopants to the solution used in USP. The novel spheres of YSZ, had similar structures, but due to the presence of rare-earth elements, they could resist significantly more to coarsening, maintaining porosity, as shown in Figure 26. The dopant level at this point was limited to 2%, but given the encouraging results, following tests will increase dopant concentration to 8%. Preliminary tests showed an improvement in stability of the porous structure up to 1100 °C.

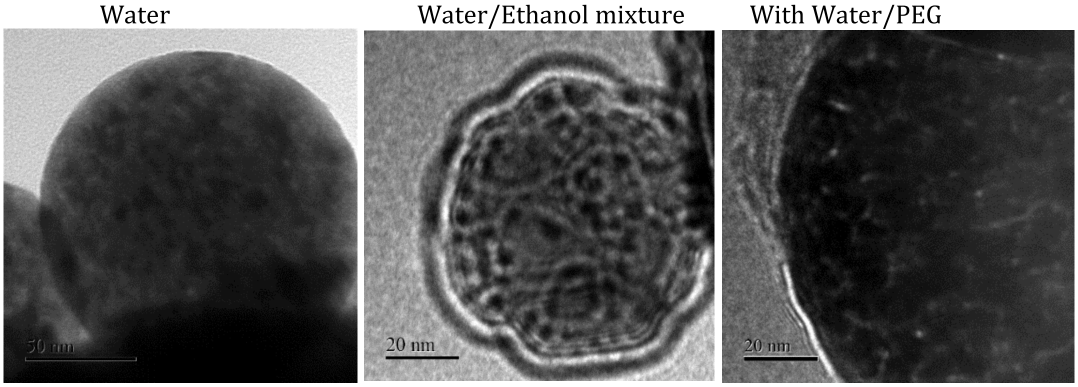

Figure 25: TEM images of YSZ synthesized at 1100 °C.

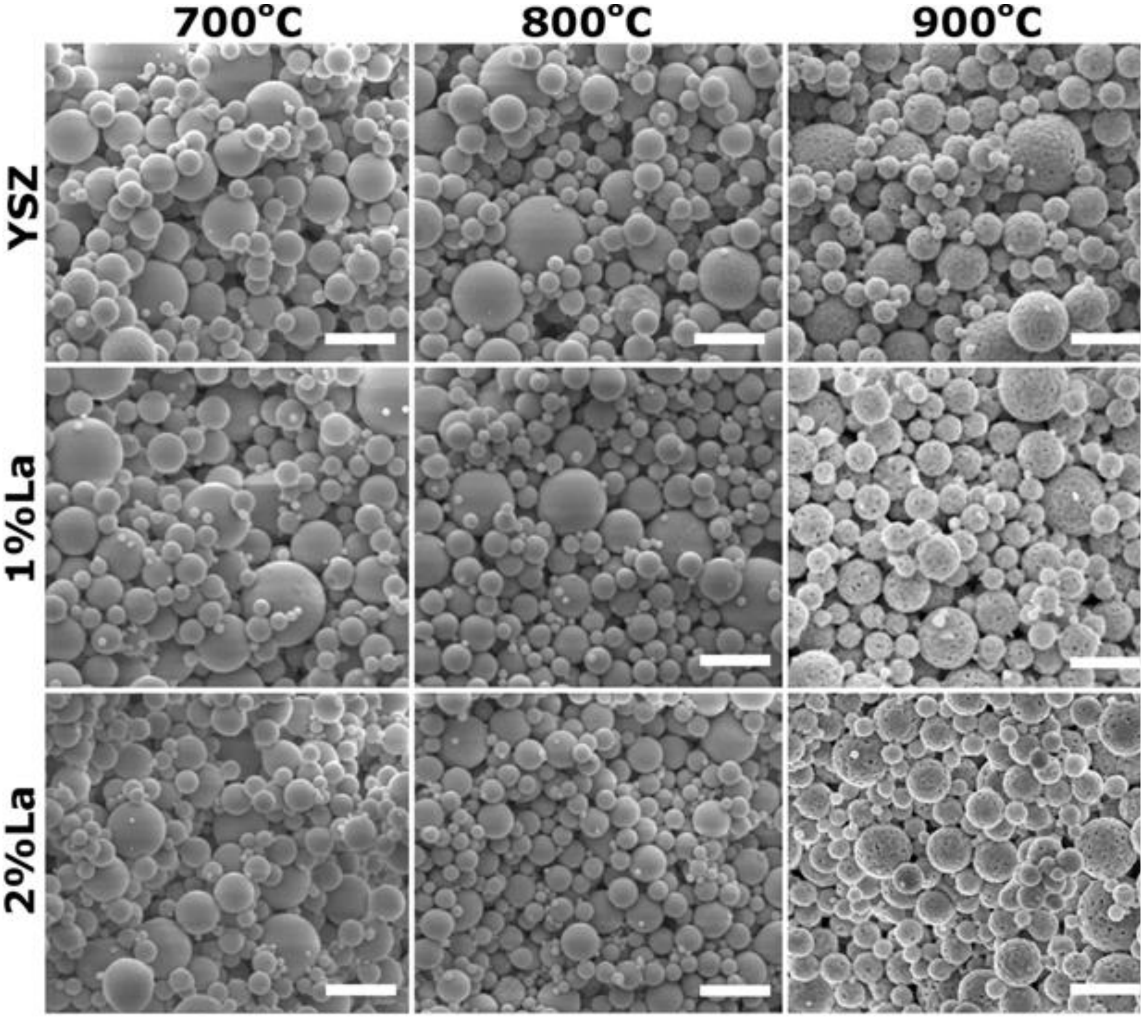

Fig. 26 SEM micrograph of YSZ and La-doped YSZ after annealing. The scale bars correspond to 1 micron. The images shall be read as in a table, with column and row corresponding to specific composition and temperature. All annealing times are 3h.

We also performed proof-of-principle experiments to demonstrate the utility of the particle ALD approach with alumina deposited on nickel particles (Figure 9) representing uranium oxide fuel particles. Nickel and uranium oxide have negligible solubility for helium, an important fission gas product. The high surface to volume ratio of the nickel particles we employed for our experiments enables us to sensitively probe the properties of surface-deposited alumina layer. Alumina is chemically compatible with uranium oxide, easily formed by particle ALD, and some phases of alumina have significant He solubility. We loaded helium at 800C into alumina-coated Ni particles, and quantitatively observed the evolution of He as a function of heating to 1400 C. Our results suggest that amorphous phases of alumina may be effective for controlled transport of He, but when crystallized above 800 C, this functionality is likely lost.

.

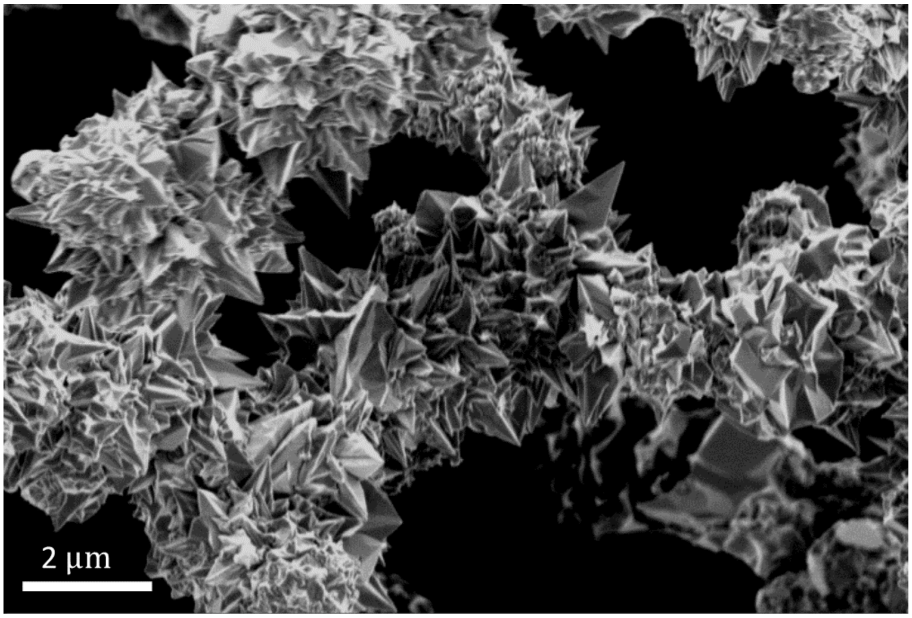

Figure 27 Nickel particles used as surrogates for uranium oxide to study of ALD alumina as a demonstration material for capture and transport of helium, a fission product gas

We have also identified a lack of fundamental understanding on how to maintain porous structures stable under extreme environments, such as high temperatures, pressures and radiation. Therefore, we have been working on both experimental and simulations to understanding how to design, from an atomistic perspective, a truly stable structure. In principle, sintering of porous structures is responsible for its collapsing at high temperatures. The driving force for sintering is related to both surface energy and GB energy [14-15], and the change in the free energy along the process can be described as:

$$\delta G_{sys} = \delta\int \gamma_S dA_S + \delta\int \gamma_{GB} dA_{GB}$$

where G_{sys} is the total interfacial energy of the system, A_S is the specific free surface area, and A_{GB} is the GB area. Moreover, the GB energy relates to the surface energy through Young's relation:

$$\frac{\gamma_{GB}}{\gamma_S} = 2\cos\left(\frac{\phi_e}{2}\right)$$

MOLECULAR SIMULATION

Mesoporous silica nanoparticles simulations (for type MCM-41)

A mesoporous silica MCM-41 model has been generated using random insertion method in Lammps software. The parameters are shown in the left part in Figure 28, with pore diameter equals to 2.8 nm. The amorphous skeleton structure has been characterized by radial distribution function and is comparable to literature's results. The pores have been created by deleting atoms at the corresponding region while the atomic ratio of silicon to oxygen is kept to 1:2. The pore surface is energetically heterogeneous and we use this model for gas adsorption studies.

Structural evolution with increasing temperature from 300 K to 5000 K has also been studied to better understand the possible thermal degradation process, as shown in the right part of Fig. 28. As can be seen, the pore structure will tend to collapse when the temperature increases, and finally becomes too small to adsorb gas molecules. One thing worth mentioning is that the melting rate used in simulation is 1 K/ps, which is much faster than in any real situations. So the degradation process is not quantitatively correct, i.e., the critical collapse temperature shown here around 2600 K is actually much higher than in a real situation (which is around 1000 °C). However, it can still qualitatively reflect the degradation process.

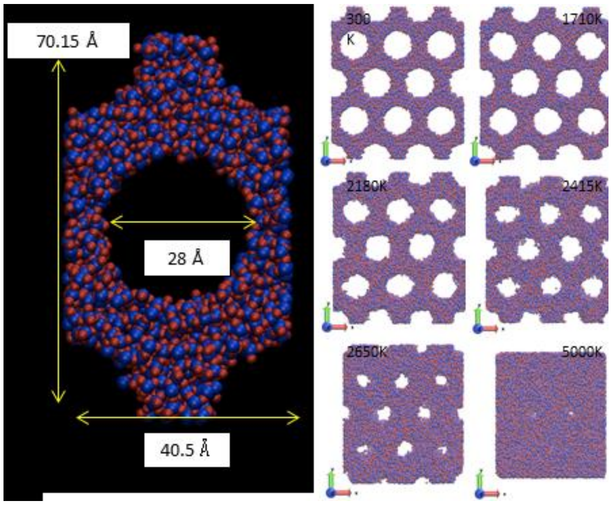

Figure 28. Left: Simulation model of one unit cell of mesoporous silica MCM-41 at 300 K with NVT condition, the blue atom represents silicon and the red atom represents oxygen. The predefined geometry is shown in the figure (20 Å in z) . Right: structure evolution with increasing temperature from 300 K to 5000 K at constant pressure (1 bar).

A calculations on gas adsorption and comparison to our data is shown in Fig. 29. The fit to data is reasonable compared to other simulations in the literature.

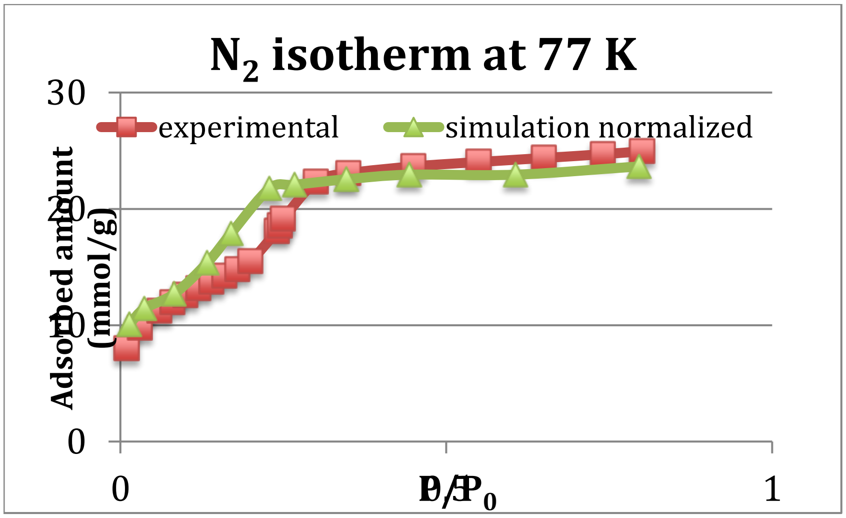

Figure 29. Simulaton and comparison to our data of nitrogen gas adsorption at 77 K for mesoporous silica nanoparticles.

A detailed study on the thermal stability of mesoporous silica MCM-41 using molecular dynamics method has been carried out. Independent structures heated at 1273 K, 1773 K, 2180 K and 2415 K for 20 ns have been generated and characterized including radial density profile (Fig. 30) , Si-O-Si bond angle distribution, radial distribution function and matrix density (Fig. 31 and Table 13). In addition, nitrogen gas adsorption is calculated in heat treated MSN-41 (Fig. 32).

Based on these studies, we propose a thermal degradation mechanism of the MCM-41 structure. Firstly, the material undergoes a compression stage towards the porous region. Then, when the temperature is high enough, the kinetic energy allows atoms to diffuse into the porous region. We concluded that surface tension and curvature of pores are the two main driving forces for the closure of the pores at high temperature.

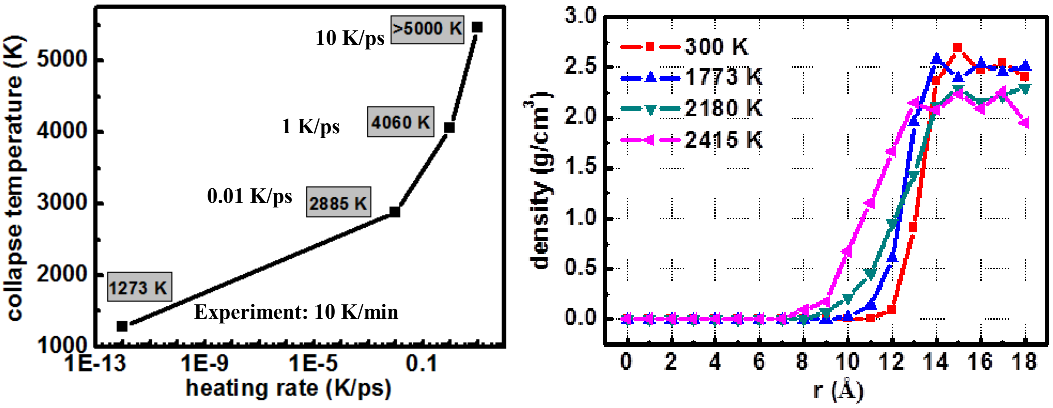

Figure 30. Left: temperature at which the MCM-41 porous model collapses, and it is influenced by the heating rate applied during simulation. The faster the heating rate is, the higher the collapse temperature would be. Right: radial density profile of models heated at corresponding temperature. The pore radius keeps decreasing, and after 2180

K, the interfacial region becomes larger, indicating the diffusion of surface atoms into the porous region.

	300 K	1273 K	1773 K	2180 K	2415 K
radial distance (Å)	13.7	13.5	13	12	11
oxygen calculated	59	52	73	57	59
CN=1	33	25	9	5	2
CN=2	26	27	63	55	57
CN=1 ratio (%)	44%	48%	14%	4%	3%

Table 13: coordination number (CN) characterization of oxygen atoms at the surface of MCM-41 structure heated to different temperatures. This reflects the decrease of oxygen dangling bonds at the surface during thermal treatment.

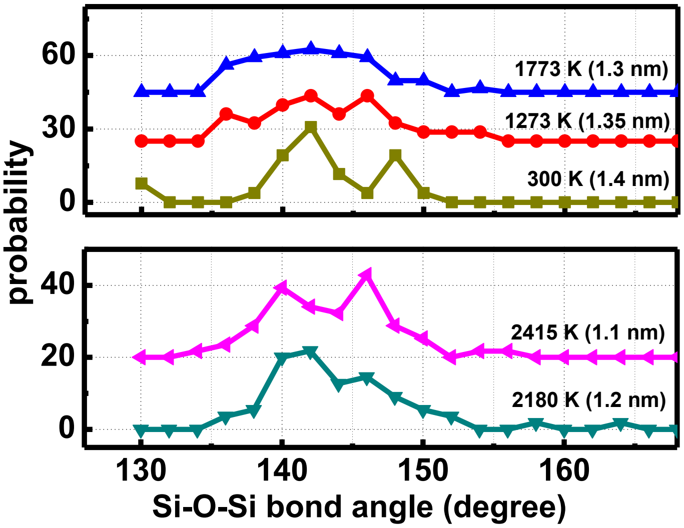

Figure 31. Si-O-Si bond angle distribution near pore surface. The number in the bracket means the radial distance from the center of the pore.

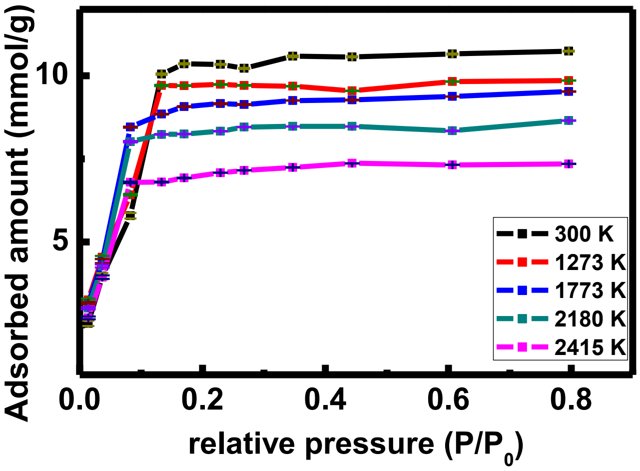

Figure 32. Nitrogen gas adsorption simulation at 77 K by structures heated to different temperatures

Molecular Modeling of Boron Nitride Nanotubes (BNNT) and Nanosheets (BNNS)

Quantum mechanics computations have been performed to calculate the interaction energies between BNNT, BNNS and noble gases. Density functional theory was applied with various choices of functional and basis sets. Potential energy surface (PES) of noble gases apart from the BNNS surface has been studied for multiple cases.

The BNNS model used in current work consists of 36 atoms in total. B-N bond length was set as 1.446 Å. The empty bands on the edge of the nanosheet were filled with hydrogen atoms. Ar atom was used for the current tests. The simulation model of BNNS with Ar is shown in Fig. 33.

The potential energy surface (PES) between Ar and BNNS has been studied with different functionals and compared with data collected with existing empirical force fields, as shown in Fig. 34. The B3LYP, as one of the most common functional used in DFT calculations, does not have dispersion correction terms and presents low adsorption at relatively long distances. The wB97XD functional, which has dispersion and long-range correction terms, improved the potential curve. The data collected from empirical force field fit well with the wB97XD functional data in long distance, but presents stronger repulsion in short distance.

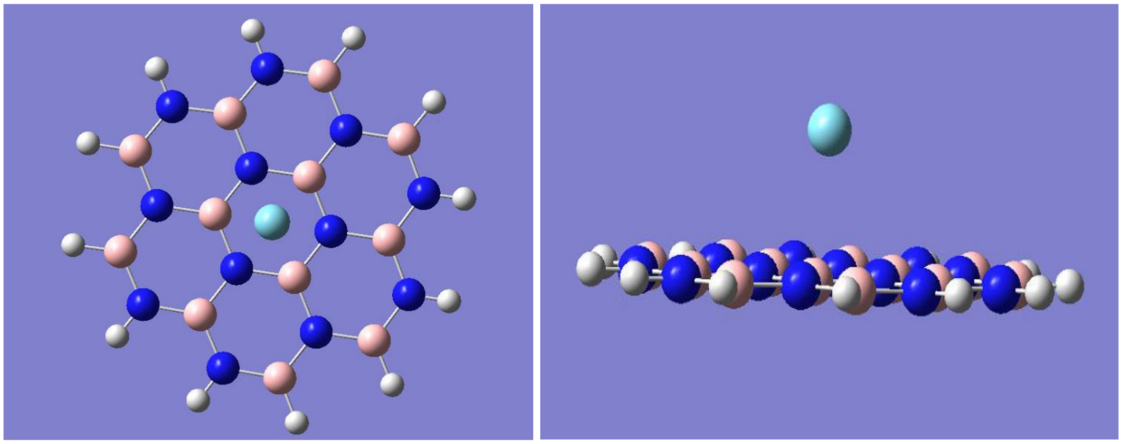

Fig. 33. Boron nitride nanosheet and noble gas simulation model

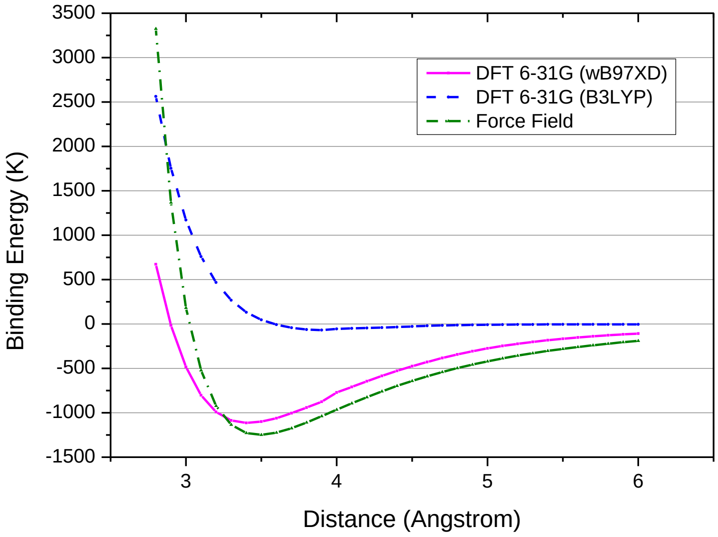

Fig. 34. Potential energy surface study of different functionals and empirical force field

Furthermore, the effect of basis set used in DFT calculations was also tested and plotted in Fig. 35. Three basis sets including 3-21G, 6-31G(d) and 6-311G(d,p) were selected where the accuracy increases with higher-level basis sets. The 3-21G, with the least Gaussian type orbitals for calculation, gave the strongest interaction. The 6-31G(d) shows comparable data with the highest-level basis set (6-311G(d,p)) used in the study.

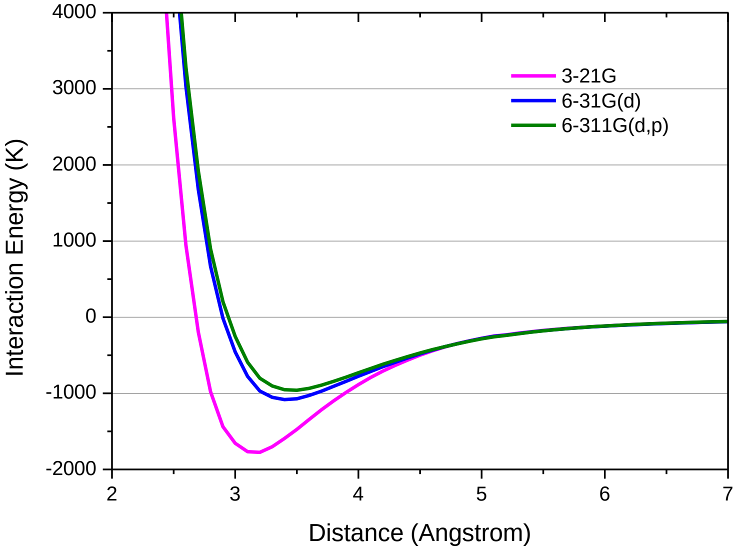

Fig. 35. Basis set effects on interaction energy

PES of different binding sites on the BNNS, was also compared. Binding sites of nitrogen, boron and the center of the hexagonal ring were studied. PES results are plotted in Fig. 36. No significant difference is observed from the result. The center is the energy-preferred form with a slightly deeper interaction energy well.

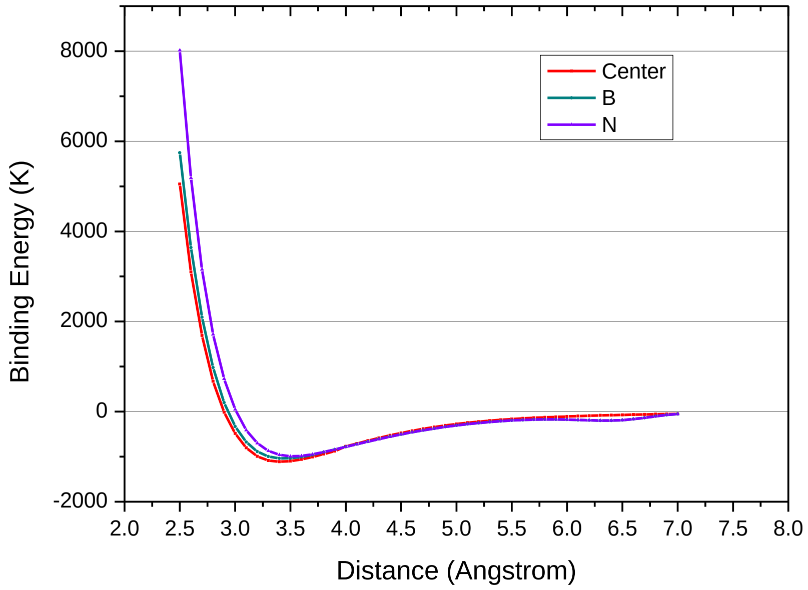

Fig. 36. Binding sites effect on interaction energy between BNNS and noble gas

Boronitride nanomaterials have been computationally investigated on the effect of the surface curvature of a Boron Nitride (BN) nanotube/nanosheet on gas adsorption. Curved boron nitride layers with different curvatures in finite sizes interacting with a number of different gases including noble gases, oxygen, and water on both their convex and concave sides of the surface were studied using density functional theory (DFT) with a high level dispersion corrected functional. Potential energy surfaces of the gas molecules interacting with the selected BN surfaces were investigated.

In addition, the charge distribution and electrostatic potential contour of the selected BN surfaces are discussed. The results reveal how the curvature of the BN surfaces affects gas adsorption. In particular, small curvatures lead to a slight difference in the physisorption energy, while large curvatures present distinct potential energy surfaces, especially for the short-range repulsion.

Carbon based nanomaterials

Besides BN nanomaterials, novel layered carbon material – Carbon Nanoscroll (CNS), which has a similar structure as multiwall carbon nanotube, but with potentially adjustable interlayer distance (as shown in Fig. 37), has also been studied on gas adsorption properties utilizing both molecular dynamics and Monte Carlo methods. Gas adsorption simulations were performed on both pure noble gases and noble gas mixtures. Figure 38 shows the adsorption isotherms at varying CNS interlayer distance at 300 K and 1 bar. By increasing interlayer distance, gas atoms with larger atomic size and stronger interaction with CNS are more adsorbed and eventually dropped when the distance is further enlarged.

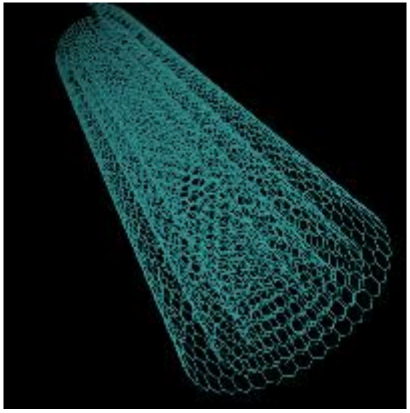

Figure 37. Model of Carbon nanoscroll

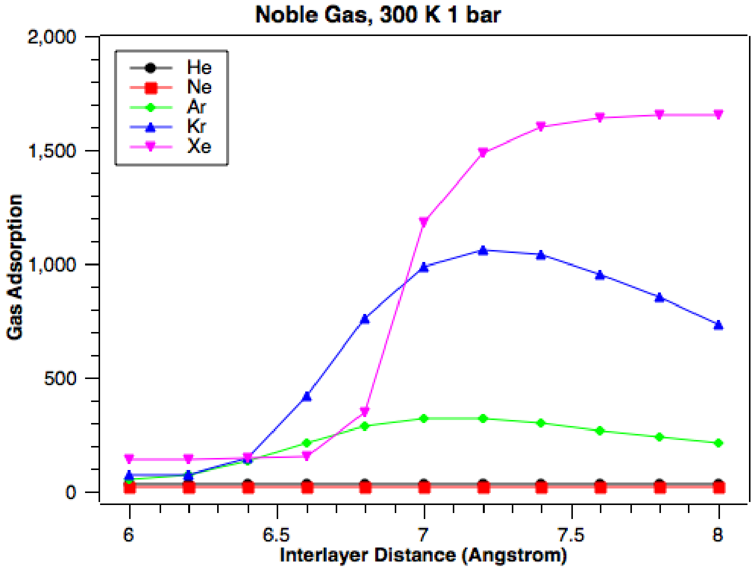

Figure 38. Noble gas adsorption on CNS with varying carbon interlayer distance at 300 K, 1 bar

Binary noble gas mixtures were also tested on our simulation model at 300 K and 1 bar. Adsorption data was analyzed with radial distribution function (RDF) as shown in Fig. 39 and the corresponding simulation snapshots are shown in Fig. 39 insets. By changing up the CNS interlayer distance, selective adsorption effect can be clearly observed at a specific window, which indicates the potential application in molecular sieving.

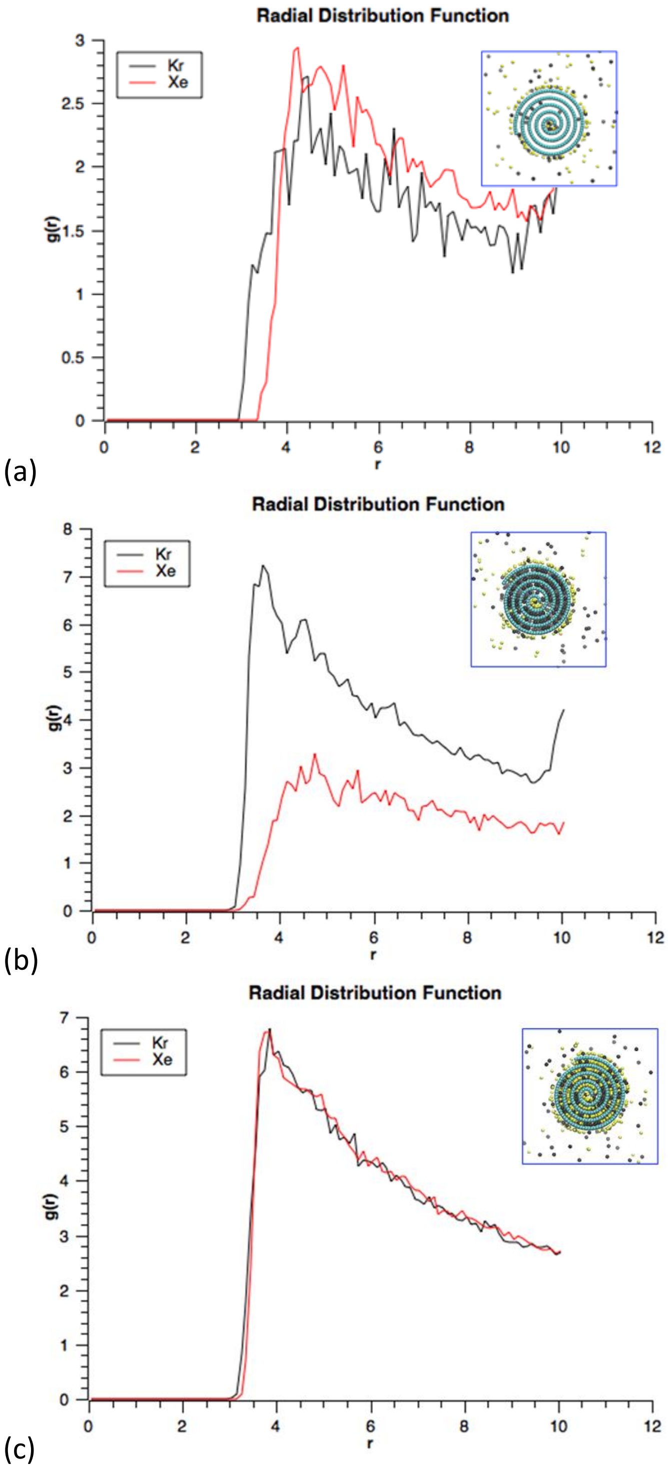

Figure 39. Binary noble gas mixture (Kr – Xe) adsorption on CNS with varying interlayer distance at 300 K, 1 bar: (a) 6.2 Å, (b) 6.6 Å, (c) 7.0 Å (inlet: simulation snapshot)

Yttria-Stabilized Zirconia

High yield synthesis of yttria-stabilized zirconia (YSZ) porous microspheres can be used in advanced thermal barrier coatings, exploiting reflective properties originated from high temperature photonics. The complexity of typical wet-chemistry processes utilized in microspheres manufacturing limits yield and can hardly deliver stable porous structures. Here, ultrasonic spray pyrolysis was utilized to produce high quantities of porous YSZ. Droplets of an aqueous precursor solution were dragged with continuous air flow into a furnace kept at temperatures varying from 700 to 1200 °C. Spherical fully cubic zirconia particles were obtained in all processing conditions, and the sizes of the spheres decreased as a function of the processing temperature, ranging from 484 to 373 nm (average diameters), while their crystallite sizes had an inverse trend, ranging from 4.9 to 25.2 nm. This was attributed to higher temperatures activating coarsening of the spheres.

The mechanical property of ceramic materials such as yttria-stabilized zirconia (YSZ), which can be potentially used in high-temperature operating environment, is greatly influenced by its grain boundary energy. Here we mainly used molecular dynamics simulation and Monte Carlo simulation to show how the grain boundary energy can be controlled by doping aliovalent cations, including La^{3+} and Gd^{3+}.

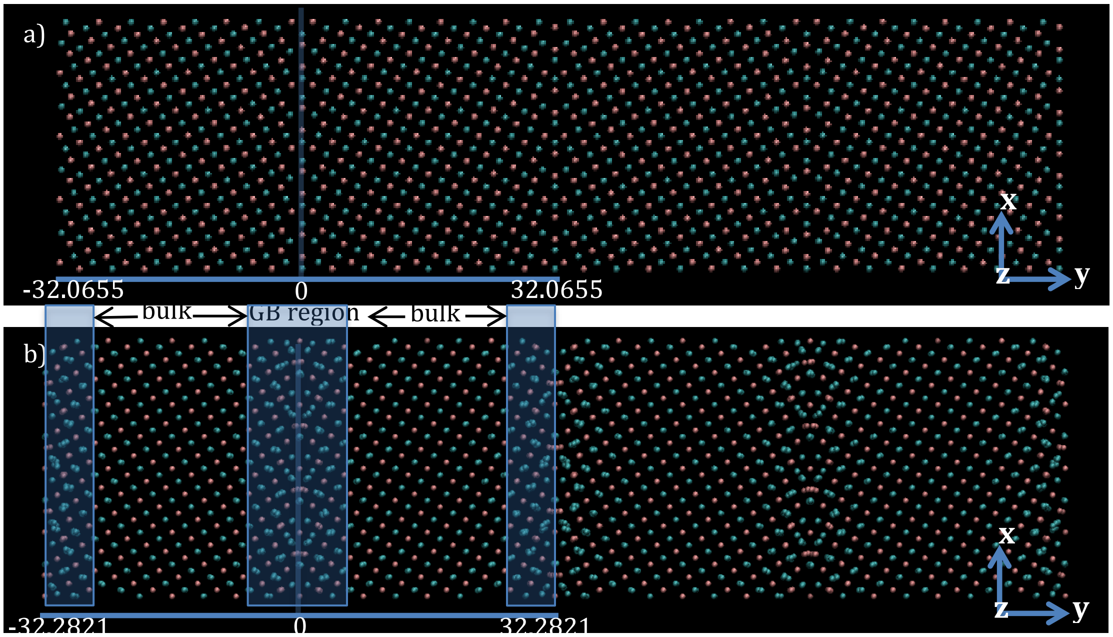

Figure 40 Σ5 (310)/[001] ZrO_2 GB model, green:Zr, red: O. a) before minimization b) after minimization, shaded blue area is considered as GB region.

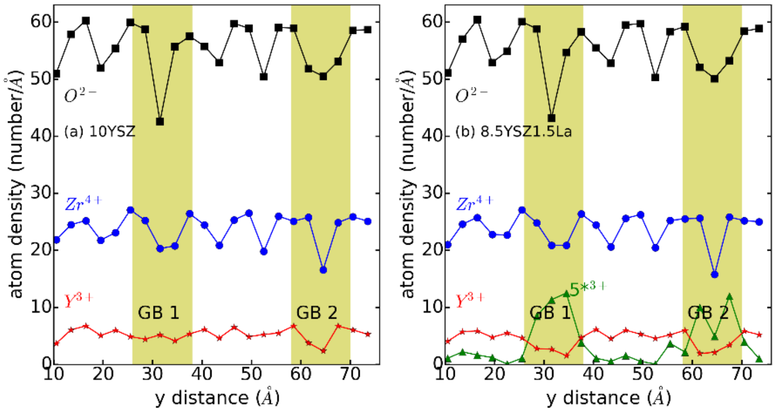

Figure 41 Atomic density (number/ Å) profile at T=300 K after MC simulation. The y coordinates have been shifted to avoid visualizing the GB region at the boundary. The GB region is the same as defined in Fig.1 and shaded with yellow color. a) 10 molar percent Y_2O_3 doping. b) 8.5 molar percent Y_2O_3 and 1.5 molar percent La_2O_3 doping.

Y^{3+} serves as a stabilization dopant and won't segregate at grain boundary, while La^{3+} and Gd^{3+} will segregate, instead of forming a second phase in YSZ.

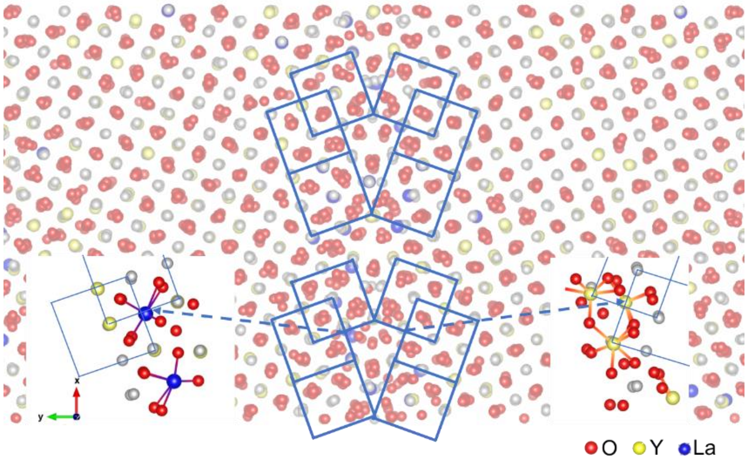

Figure 42 Zoomed-in grain boundary region to show La-O and Y-O bonding configurations in 8.5Y1.5La doping case.

By comparing La^{3+} and Y^{3+} at similar sites at grain boundary region, it is found La^{3+} generally forms 7 bonds with O^{2-}, while Y^{3+} averagely forms 6 bonds with O^{2-}. The grain boundary energy of 8.5Y1.5La (0.69 J/m^2) thus is found to be less than 10YSZ (0.81 J/m^2).

Our results concerning the role of La on the stabilization of YSZ interfaces are very encouraging. We still have to address the effect of La on the surface, which is ongoing work. This perspective of solving the problem of thermo-stability from an energetic perspective is quite unique and we excited about the possibilities emerging from that. One nanoporous structures are stable from a thermodynamic perspective, it is apparent that even if diffusion is available, pores will not collapse. This is a mandatory function for production of pore-controlled nuclear fuel pellets.

References

1. Ferry, C.; Piron, J.-P.; Ambard, A., Effect of helium on the microstructure of spent fuel in a repository An operational approach. *Journal of Nuclear Materials* **2010,** *407* (2), 100-109.

2. Roudil, D.; Deschanels, X.; Trocellier, P.; Jegou, C.; Peuget, S.; Bart, J. M., Helium thermal diffusion in a uranium dioxide matrix. *Journal of Nuclear Materials* **2004,** *325* (2-3), 148-158.

3. Han, W.; Bando, Y.; Kurashima, K.; Sato, T., Synthesis of boron nitride nanotubes from carbon nanotubes by a substitution reaction. *Applied Physics Letters* **1998,** *73* (21), 3085-3087.

4. Golberg, D.; Bando, Y.; Kurashima, K.; Sato, T., MoO3-promoted synthesis of multi-walled BN nanotubes from C nanotube templates. *Chem. Phys. Lett.* **2000,** *323* (1–2), 185-191.

5. Campo, M. C.; Magalhaes, F. D.; Mendes, A., Comparative study between a CMS membrane and a CMS adsorbent: Part I-Morphology, adsorption equilibrium and kinetics. *Journal of Membrane Science* **2010,** *346* (1), 15-25.

6. Afolabi, A. S.; Abdulkareem, A. S.; Iyuke, S. E., Synthesis of carbon nanotubes and nanoballs by swirled floating catalyst chemical vapour deposition method. *Journal of Experimental Nanoscience* **2007,** *2* (4), 269-277.

7. Rutherford, S. W.; Do, D. D., Characterization of carbon molecular sieve 3A. *Langmuir* **2000,** *16* (18), 7245-7254.

8. Danon, A.; Finkelstein, Y.; Koresh, J. E., Sieving Effect of Neon and Helium at High Temperature on Carbon Molecular Sieve Fibers. *Langmuir* **2002,** *18* (3), 638-641.

9. Trigueiro, F.; Monteiro, D.; Zotin, F.; Falabella Sousa-Aguiar, E., Thermal stability of Y zeolites containing different rare earth cations. *Journal of alloys and compounds* **2002,** *344* (1), 337-341.

10. Tallon, J.; Buckley, R., Thermal decomposition of the zeolite catalyst ZSM-5. *Journal of Physical Chemistry* **1987,** *91* (6), 1469-1475.

11. Abbott, P. J.; Tison, S. A., Commercial helium permeation leak standards: Their properties and reliability. *Journal of Vacuum Science & Technology a-Vacuum Surfaces and Films* **1996,** *14* (3), 1242-1246.

12. Rogers, W. A.; Buritz, R. S.; Alpert, D., DIFFUSION COEFFICIENT, SOLUBILITY, AND PERMEABILITY FOR HELIUM IN GLASS. *Journal of Applied Physics* **1954,** *25* (7), 868-875.

13. Stali\circonunas, K. In *Why patterns appear spontaneously in dissipative systems?*, Nonlinear Analysis: Modelling and Control, Vilnius, IMI: Vilnius, 1999; pp 113-118.

14. Wong, B.; Pask, J. A., Models for kinetics of solid state sintering. *Journal of the American Ceramic Society* **1979,** *62* (3-4), 138-141.

15. Liu, F.; Chen, Z.; Yang, W.; Yang, C. L.; Wang, H. F.; Yang, G. C., Thermodynamics of nano-scale grain growth. *Mater. Sci. Eng. A-Struct. Mater. Prop. Microstruct. Process.* **2007,** *457* (1-2), 13-17.

16. Lange, F. F., Densification of powder compacts: An unfinished story. *J. Eur. Ceram. Soc.* **2008,** *28* (7), 1509-1516.

17. Kellett, B. J.; Lange, F. F., THERMODYNAMICS OF DENSIFICATION .1. SINTERING OF SIMPLE PARTICLE ARRAYS, EQUILIBRIUM-CONFIGURATIONS, PORE STABILITY, AND SHRINKAGE. *J. Am. Ceram. Soc.* **1989,** *72* (5), 725-734.

18. Lange, F. F.; Kellett, B. J., Thermodynamics of densification .2. Grain growth in porous compacts and relation to densification. *Journal of the American Ceramic Society* **1989,** *72* (5), 735-741.

19. Wakai, F.; Yoshida, M.; Kashyap, B. P., Influence of particle arrangement on coarsening during sintering of three spherical particles. *Journal of the Ceramic Society of Japan* **2006,** *114* (1335), 974-978.

20. Wakai, F.; Yoshida, M.; Shinoda, Y.; Akatsu, T., Coarsening and grain growth in sintering of two particles of different sizes. *Acta Materialia* **2005,** *53* (5), 1361-1371.

21. Buban, J. P.; Matsunaga, K.; Chen, J.; Shibata, N.; Ching, W. Y.; Yamamoto, T.; Ikuhara, Y., Grain boundary strengthening in alumina by rare earth impurities. *Science* **2006,** *311* (5758), 212-215.

PUBLICATIONS

Kelly Guan, **Gas uptake and thermal stability analysis of boron nitride and carbon nanotubes,** MS thesis, September 2015, UC Davis.

Hoayan Sha, **Molecular Simulation of Gas Interactions with Complex Materials,** PhD Thesis, September 2017, UC Davis

Haoyan Sha, Roland Faller: **Quantum Chemistry Study of Curvature Effects on Boron Nitride Nanotube/Nanosheet for Gas Adsorption** *Phys Chem Chem Phys* **18(29)** 19944-19949 (2016)

Haoyan Sha, Roland Faller: **Molecular Simulation of Adsorption and Separation of Pure Noble Gases and Noble Gas Mixtures on Single Wall Carbon Nanotubes** *Computational Materials Science* **114** 160-166 (2016)

Shenli Zhang, Maria Perez-Page, Kelly Guan, Erick Yu, Joseph Tringe, Ricardo Castro, Roland Faller, Pieter Stroeve: **Response to Extreme Temperatures of Mesoporous Silica MCM-41: Porous Structure Transformation Simulation and Modification of Gas Adsorption Properties** *Langmuir* **32 (44)**, 11422–11431 (2016)

María Pérez-Page, James Makel, Kelly Guan, Shenli Zhang, Joseph Tringe, Ricardo H.R. Castro, Pieter Stroeve **Gas adsorption properties of ZSM-5 zeolites heated to extreme temperatures,** *Ceramics International,* **42(14)**, 15423-15431 (2016)

Nazia Nafsin, Hui Li, Elisabeth W. Leib, Tobias Vossmeyer, Pieter Stroeve, Ricardo H. R. Castro **Stability of rare-earth-doped spherical yttria-stabilized zirconia synthesized by ultrasonic spray pyrolysis** *J Amer Ceram Soc* **100 (10)** 4425-4434 (2017)

Maria Perez-Page, Ryan Guzalowski, Dereck N.F. Muche, Ricardo H.R. Castro, Pieter Stroeve **Synthesis of porous yttria-stabilized zirconia microspheres by ultrasonic spray pyrolysis** *Materials Letters* **188**, 41–44 (2017)

Shenli Zhang, Haoyan Sha, Erick Yu, Maria Perez Page, Ricardo Castro, Pieter Stroeve, Joseph Tringe, and Roland Faller: **Computational and Experimental Studies on Novel Materials for Fission Gas Capture** in *Proceedings: 18th International Conference on Environmental Degradation of Materials in Nuclear Power Systems – Water Reactors* (Editors: John Jackson, Denise Paraventi, Michael Wright) Page 1039-1050 (2017)

Shenli Zhang, Erick Yu, Sean Gates, William Cassata, James Makel, Andrew M. Thron, Christopher Bartel, Alan W. Weimer, Roland Faller, Pieter Stroeve and Joseph Tringe: **Helium interactions with alumina formed by atomic layer deposition show potential for mitigating problems with excess helium in spent nuclear fuel** *J Nucl Mat* **499** 301-311 (2018)

Saeed Kamali, Eugenio Bringas, Hien-Yoong Hah, Brian Bates, Jacqueline A. Johnson, Charles E. Johnson, Pieter Stroeve: **Magnetism and Mössbauer study of formation of multi-core γ-Fe_2O_3 nanoparticles** *Journal of Magnetism and Magnetic Materials* **451** 131–136 (2018)

Haoyan Sha, Shenli Zhang, Roland Faller: **Molecular Investigation of Gas Adsorption, Separation, and Transport on Carbon Nanoscrolls: A Combined Grand Canonical Monte Carlo and Molecular Dynamics Study** *Carbon* **132** 401-410 (2018)

Shenli Zhang, Haoyan Sha, Ricardo Castro, Roland Faller: **Atomistic modeling of La3$^+$ doping segregation effect on nanocrystalline yttria-stabilized zirconia** *Phys Chem Chem Phys* in press (DOI 10.1039/C8CP02010H)

Arseniy Bokov, Shenli Zhang, Shen J. Dillon, Lin Feng, Roland Faller, Ricardo H. R. Castro: **Energetic design of grain boundary networks for toughening of nanocrystalline oxides** submitted

Haoyan Sha, Shenli Zhang, Roland Faller: **Molecular Dynamics Insight in the Tilt Effect of Carbon Nanotubes in Small Assemblies** submitted